

Review

Recent Advances in Electrocatalysts for Ammonia Oxidation Reaction

Ji Hee Jang¹, So Young Park¹, Duck Hyun Youn^{2,*}  and Youn Jeong Jang^{1,*} 

¹ Department of Chemical Engineering, Hanyang University, 222 Wangsimni-ro, Seongdong-gu, Seoul 04763, Republic of Korea

² Department of Chemical Engineering, Kangwon National University, Chuncheon 24341, Republic of Korea

* Correspondence: youndh@kangwon.ac.kr (D.H.Y.); yjang53@hanyang.ac.kr (Y.J.J.)

Abstract: Ammonia (NH₃) is a clean energy source that can either be directly used as fuel or a hydrogen carrier due to its high energy density and high hydrogen content. The NH₃ electro-oxidation reaction (AOR) is the main reaction in both direct NH₃ fuel cells and NH₃ electrolysis. The AOR is thermodynamically favorable; however, the sluggish kinetics of the reaction can result in issues such as high overpotential, slow reaction rate, deactivation, etc. To overcome this, multiple strategies have been discussed to develop electrocatalysts that maintain a robust reaction rate in low overpotential regions. In this review, the fundamentals of AOR, including thermodynamics, kinetics, and experimental techniques, are studied. This review also focused on recent progress for catalyst modifications and their effects, with a particular focus on Pt- or Ni-based electrocatalysts. Additionally, vacant rooms needed to be developed was pointed, and a way to overcome the limitations was suggested. The fundamentals and efforts to prepare catalysts reviewed in this work will be effective in proposing and designing new robust electrocatalysts leading to advance AOR in practice.

Keywords: electrocatalyst; ammonia oxidation reaction; hydrogen; nitrogen; ammonia decomposition



Citation: Jang, J.H.; Park, S.Y.; Youn, D.H.; Jang, Y.J. Recent Advances in Electrocatalysts for Ammonia Oxidation Reaction. *Catalysts* **2023**, *13*, 803. <https://doi.org/10.3390/catal13050803>

Academic Editors: Eun Duck Park, Won Bae Kim and Ji-Wook Jang

Received: 8 March 2023

Revised: 14 April 2023

Accepted: 24 April 2023

Published: 26 April 2023



Copyright: © 2023 by the authors. Licensee MDPI, Basel, Switzerland. This article is an open access article distributed under the terms and conditions of the Creative Commons Attribution (CC BY) license (<https://creativecommons.org/licenses/by/4.0/>).

1. Introduction

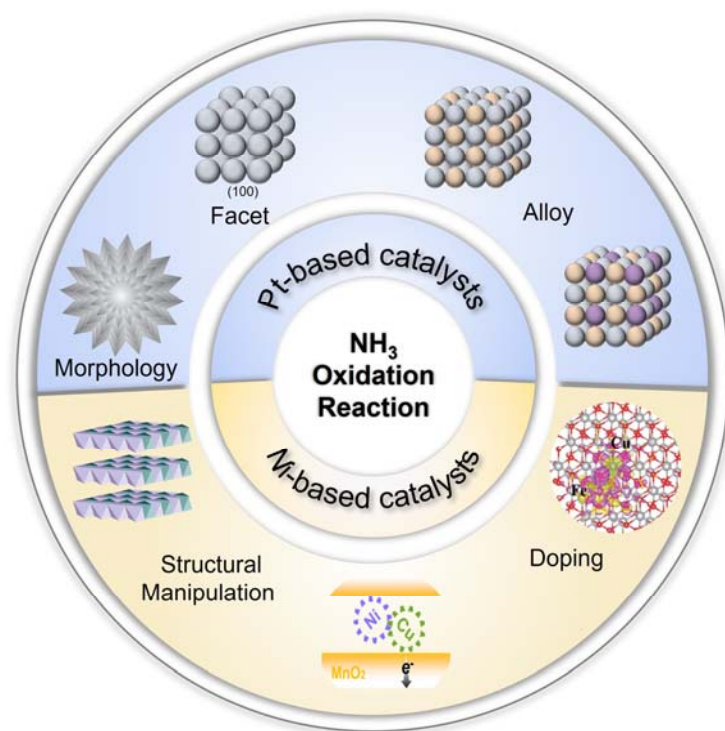
Ammonia (NH₃) is the most potential carbon-free energy carrier due to its remarkable hydrogen storage capacity (17.7 wt%) and energy density (3000 Wh kg⁻¹). Additionally, NH₃ can be effectively liquefied at ambient temperature and mild pressure under 8 bar, which makes it superior in terms of storage and transportation compared to other hydrogen carriers [1–3]. Furthermore, contrary to the traditional Haber-Bosch process, the synthesis of NH₃ using a clean electrochemical approach resulted in a decrease in CO₂ emission, which makes NH₃ a sustainable hydrogen transport media and carbon-free fuel itself [4–9].

With increasing attention to NH₃ as a green energy source, various reactions, such as NH₃ oxidation and decomposition, have been actively studied [10–15]. The use of NH₃ can be mainly divided into two ways; one is to produce electricity by directly feeding it as a fuel like methanol and hydrogen in the fuel cell, and the other is to produce hydrogen via its electrolysis [16,17]. Considering the standard reduction potential for the NH₃ oxidation and reduction ($N_2 + 6H_2O + 6e^- \rightarrow 2NH_3 + 6OH^-$, $E^\circ = -0.77 V$ vs. SHE) relative to that for the hydrogen ($2H^+ + 2e^- \rightarrow H_2$, $E^\circ = 0.00 V$ vs. SHE) required for operating in both energy devices, it has a great benefit not only as a fuel but also as a hydrogen carrier. For example, the theoretical minimal cell potential for hydrogen production in NH₃ electrolysis, requiring 0.06 V, is much smaller than the value in water electrolysis, requiring 1.23 V [18,19].

With these considerations, it is no doubt that robust electrochemical direct NH₃ oxidation (AOR, Ammonia oxidation reaction) is critical to use NH₃ in diverse energy conversion devices. Despite the thermodynamic advantage of AOR, its fundamental challenges associated with AOR include sluggish kinetics involving multiple rate-determining steps, unintentional side reactions, and irreversible reactions, such as poisoning [20–22]. Thus,

this AOR mainly suffers from large overpotentials, imperfect faradaic efficiency, and low reaction rates and stability. To overcome those challenges, active catalyst candidates have been proposed based on noble metals (Pt, Ir, Pt-based alloy, etc.), transition metals (Ni, Cu, Co, etc.), and so on [18,23–25].

In this mini-review, at first, we mainly discuss essential AOR fundamentals, including thermodynamics, kinetics corresponding to reaction mechanisms, and experimental techniques. Then, we review recent advances in catalyst design using Pt- and Ni-based electrocatalysts, showing strong progress for AOR, in more detail. Finally, we end this review by providing prospects and perspectives in terms of catalyst design and additional engineering as shown in Scheme 1. We believe that the insight and discussion for the recent achievements discussed in this mini-review will serve as useful resources for the further development of more practical and efficient AOR.

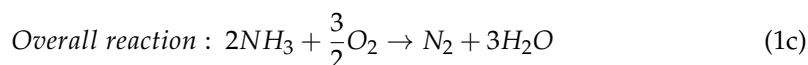
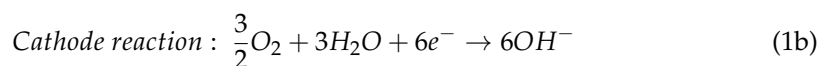
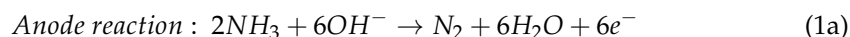


Scheme 1. Schematic diagram of NH_3 oxidation reaction performance improvement strategies covered in this paper. Schematic of Structural Manipulation: Reproduced with permission [26]. Copyright 2021, American Chemical Society. Schematic of Doping: Reproduced with permission [27]. Copyright 2021, Wiley–VCH.

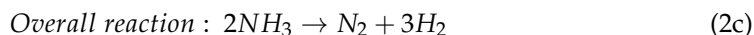
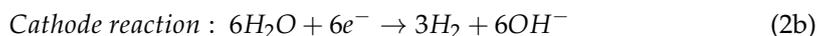
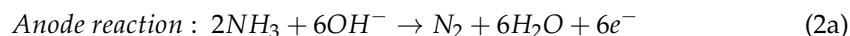
2. Fundamentals of Ammonia Oxidation

NH_3 can be used as a fuel directly in NH_3 fuel cells, and furthermore, it can be utilized as a hydrogen carrier to produce hydrogen fuel in NH_3 electrolytic cells, as shown below [16,28]:

NH_3 Fuel cell



NH_3 Electrolytic cell



Notably, NH_3 oxidation reaction (Ammonia oxidation reaction, AOR) seems to be the determining factor in regards to the overall performance of both electrochemical energy conversion devices. Thus, the robust reaction under low overpotential is the most important to develop energy applications using NH_3 .

In the Pourbaix diagram for $\text{N}_2\text{-H}_2\text{O}$ in Figure 1a, thermodynamic behavior for AOR depending on pH and potential is discussed [9]. The red line represents the theoretical standard reduction potential for the reduction of N_2 , which corresponds to the required potential for the NH_3 oxidation to N_2 and H_2 . In the universal pH range, AOR is more thermodynamically favorable than the oxygen evolution reaction (OER), and thus, the challenges coming from the competitive reaction of OER seem not to be dominant. However, experimental observations have shown significant gaps from this theoretical expectation due to extremely high overpotential requirements. Thus, in fact, experimental AOR can be competitive with OER; furthermore, the produced oxygen can additionally oxygenate undesired nitrogen species of N_2O , NO , and so on [29,30]. These challenges can be expected based on kinetic limitations for AOR.

The reaction steps include 6 electrons releasing accompanied with 2 NH_3 molecules and OH^- anions converting to N_2 and 3 H_2 molecules in alkaline media, which have been expected in two different ways, as shown in Figure 1b. In the Oswin-Salomon mechanism, an NH_3 molecule ($\text{NH}_{3,\text{ads}}$) is adsorbed onto the surface of catalysts and is further oxidized to be an adsorbed N atom (N_{ads}) with releasing electrons [31]. Finally, the two N_{ads} atoms are recombined together to form an N_2 molecule, which subsequently desorbs from the catalyst surface. However, this reaction pathway is limited by two main factors; at low current densities, the rate-determining step is the dehydrogenation reaction from $\text{NH}_{2,\text{ads}}$ to NH_{ads} ; at high current densities, the recombination of two N_{ads} becomes the rate-determining step. Additionally, the strongly adsorbed N_{ads} on the catalyst surface can cause catalyst poisoning.

On the other hand, Gerischer and Mauerer proposed another mechanism (Gerischer-Mauerer mechanism), where the first step is the dehydrogenation of $\text{NH}_{3,\text{ads}}$ to $\text{NH}_{x,\text{ads}}$ ($x = 1$ or 2) intermediates using OH^- with releasing electrons [32]. The obvious difference between this mechanism and the Oswin-Salomon mechanism is that the two dehydrogenated $\text{NH}_{x,\text{ads}}$ molecules are dimerized and then further dehydrogenated into $\text{N}_{2,\text{ads}}$. Generally, dimerization is the most representative sluggish step for AOR [20,21]. Experimental reports especially using Pt catalysts, mainly support AOR mechanisms using the Gerischer-Mauerer suggestions [1,20,33].

Meanwhile, in order to directly interpret experimental observations, including intermediates and by-product formation and catalyst deactivation, recently, extended AOR mechanisms have been proposed based on theoretical calculation and experimental observations, as shown in Figure 1c [34]. The intermediate of N_2H_{x+y} proposed in the Gerischer-Mauerer mechanism for N_2 production was experimentally revealed by in-situ/operando measurements using FTIR, ATR-SEIRAS, and online electrochemical MS [2,35,36]. Although the pathway of NO_x formation, causing catalyst poisoning, has not been clearly identified yet, their formation during AOR under high overpotential was also experimentally revealed using in-situ techniques [37].

Besides the theoretical fundamentals of AORs, it is also important to use basic experimental techniques to evaluate the performance of the reaction. The electrochemical activity, e.g., the current density, is investigated using cyclic voltammetry (CV) with a conventional three-electrode configuration (using a working electrode, a reference electrode, and a counter electrode). Figure 1d represents a CV plot obtained using a Pt working

electrode measured in 1 M KOH electrolyte with NH_4^+ (red line) and without NH_4^+ (black line). In the case of electrolytes without NH_4^+ , peaks are observed attributing to hydrogen desorption in 0.05–0.45 V_{RHE} and Pt surface oxidation from 0.45 V_{RHE} while anodic scanning. Notably, peaks representing hydrogen adsorption and Pt oxide reduction were observed during the cathodic scanning [38,39]. Interestingly, in the case of electrolytes with NH_4^+ , a distinct oxidation peak is observed at 0.45 V_{RHE} and the maximum current density is shown at 0.75 V_{RHE} , which suggests NH_3 oxidation has occurred [1]. The observed peak at 0.2 V_{RHE} during cathodic scanning represents the desorption of NH_3 and H_2 .

The actual amounts of NH_3 can be quantified using diverse detection tools, such as UV-vis spectrometer, ion chromatography, and so on. Typically, a colorimetric method using the indophenol blue indicator has been widely suggested [40,41]. The indicator comprising hypochlorite, phenolate, and ferricyanide catalyst turns the solution from yellow to green due to the Berthelot reaction with NH_4^+ in the solution. The collected adsorption data at 655 nm are shown in Figure 1e,f. Based on the standard calibration curve drawn using the known concentrations of NH_4^+ , the amount of NH_4^+ presented in the solution can be determined. In addition, N_2 produced by AOR is also quantitatively investigated using the gas chromatography [42]. The by-products can be quantified using the Watt and Chrisp method for N_2H_4 and Griess method for the NO_x species [43–45].

To determine the performance of AOR, the major three efficiencies must be determined using the quantified results as discussed above [40,42]. The first one is NH_3 removal efficiency (R%), which corresponds to the conversion of NH_3 to nitrogen-containing compounds as described in Equation (3), where $[\text{NH}_3]_0$ and $[\text{NH}_3]_t$ are the initial concentration of NH_3 added and remaining NH_3 in the electrolyte after electrolysis, respectively. The NH_3 removal efficiency indicates the conversion of NH_3 to all products containing N elements, for example, N_2 , NO_2^- , NO_3^- , and so on.

$$\text{NH}_3 \text{ removal efficiency, } R (\%) = \frac{[\text{NH}_3]_0 - [\text{NH}_3]_t}{[\text{NH}_3]_0} \times 100 \quad (3)$$

Another important factor is the selectivity for the NH_3 to N_2 conversion as described in Equation (4), where $[\text{N}_2]$, $[\text{NO}_3^-]$, and $[\text{NO}_2^-]$ represents the concentration of N_2 , NO_3^- , and NO_2^- able to be produced from AOR, respectively.

$$\text{Selectivity of } \text{NH}_3 - \text{N}_2 \text{ conversion, } SN (\%) = \frac{[\text{N}_2]}{[\text{NO}_2^-] + [\text{NO}_3^-] + [\text{N}_2]} \times 100 \quad (4)$$

The last one is the faradaic efficiency, which represents the performance to release electrons from NH_3 - N_2 conversion against the total amount of released electrons, is given in Equation (5). Q theoretically released e^- , indicates the overall amounts of generated electrons during potential constant electrolysis, as observed in the J-t plot, and the other Q , actually released e^- , represents the number of electrons generated from the only NH_3 - N_2 conversion. In addition, the constant of 6 indicates that 6 electrons can be generated from two NH_3 molecules to produce one N_2 molecule.

$$\text{Faradaic efficiency, } FE (\%) = \frac{6 Q \text{ actually released } e^-}{Q \text{ theoretically released } e^-} \times 100 \quad (5)$$

So far, fundamentals, challenges, experimental investigation methods, and efficiencies to determine AOR were overviewed. Considering what is discussed above, to improve the performance, strategies to design effective catalysts are highly required. In the next section, promising strategies to prepare effective electrocatalysts and how each strategy affects AOR's performances will be reviewed.

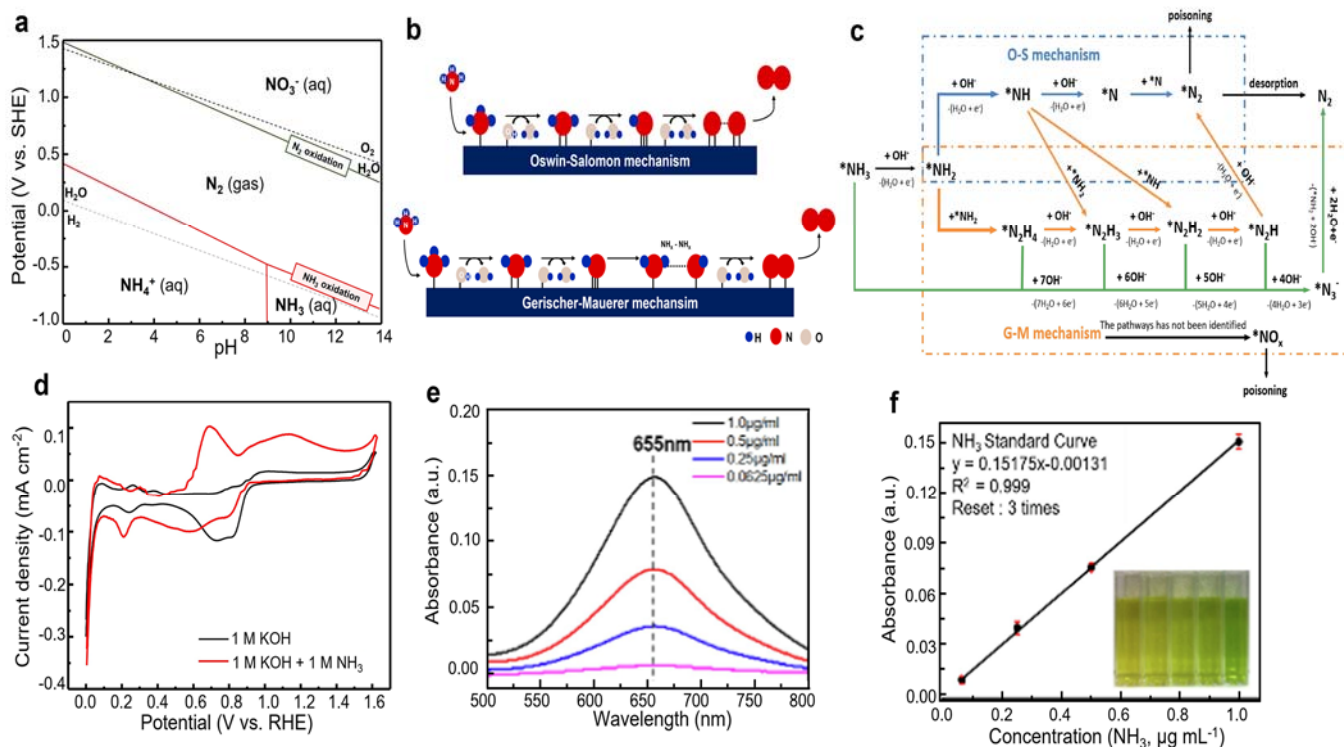


Figure 1. (a) Pourbaix diagram for the N_2 - H_2O system. Reproduced with permission [9]. Copyright 2022, MDPI. (b) Schematic diagram of the NH_3 oxidation pathways. (c) The extended AOR mechanism includes NO_x species. The O-S mechanism indicates the Oswin-Salomon mechanism, and the G-M mechanism indicates the Gerischer-Mauerer mechanism. * indicates adsorption on the catalyst surface. Reproduced with permission [34]. Copyright 2022, Elsevier B. V. (d) Cyclic voltammograms of Pt plate in the presence (red line) and absence (black line) of 0.1 M NH_3 in 1 M KOH with a scanning rate of 20 mV s^{-1} . (e) UV-Vis absorption spectra of indophenol assays with various NH_3 concentrations. (f) Calibration curve used for the NH_3 quantification. Reproduced with permission [41]. Copyright 2023, Elsevier B. V.

3. Electrocatalysts for Ammonia Oxidation

This section mainly investigates two groups of NH_3 oxidation catalysts and their performances: (1) Pt-based electrocatalysts and (2) Ni-based electrocatalysts.

3.1. Pt-Based Electrocatalysts

3.1.1. Pure Pt Electrocatalysts

Noble metals (Ru, Rh, Pd, Pt, and Ir) and transition metals (Au, Ag, and Cu) have been considered to be used as catalysts in AOR. Ru, Rh, and Pd typically have too strong of an affinity for N_{ads} to produce N_2 , whereas transition metals have relatively too weak NH_3 adsorption to dehydrogenate NH_3 [46]. However, Pt is satisfactory in terms of NH_3 adsorption and dehydrogenation capacity, $NH_{x,ads}$ dimerization and product desorption; for this reason, Pt has been considered the most active catalyst and widely studied to be used in AOR [20]. To develop the catalytic performance of Pt with reducing the disadvantage of high cost, multiple strategies have been proposed, such as morphology and shape modification, exposure facet engineering, and so on [18,47,48]. In this part, recent efforts are mainly reviewed about the way to increase surface area and to provide catalytically active facets of Pt (100). Furthermore, it is discussed how each suggestion affects AOR performance.

Guntae Kim et al. synthesized two different types of Pt electrodes, which have uneven dense morphology or flower-shape depending on electrocatalytically synthetic condition [42]. The unevenly dense shaped Pt (CP-Pt) electrode was prepared using chronopotentiometry (CP) at a constant current of 2 mA, whereas the flower-shaped Pt (X

CV-Pt, where X is the number of CV cycles; 100, 200, 300, 400, 500 and 600) electrode was deposited using cyclic voltammetry (CV) in the potential range of -0.4 to 0.2 V_{Ag/AgCl}, as shown in Figure 2a. Unlike during the CP process, H₂ bubbles are generated via water reduction while scanning potential negatively than hydrogen reduction potential during the CV process. The evolution and detachment of the H₂ bubble at a particular Pt site induce a flower-shaped Pt formation.

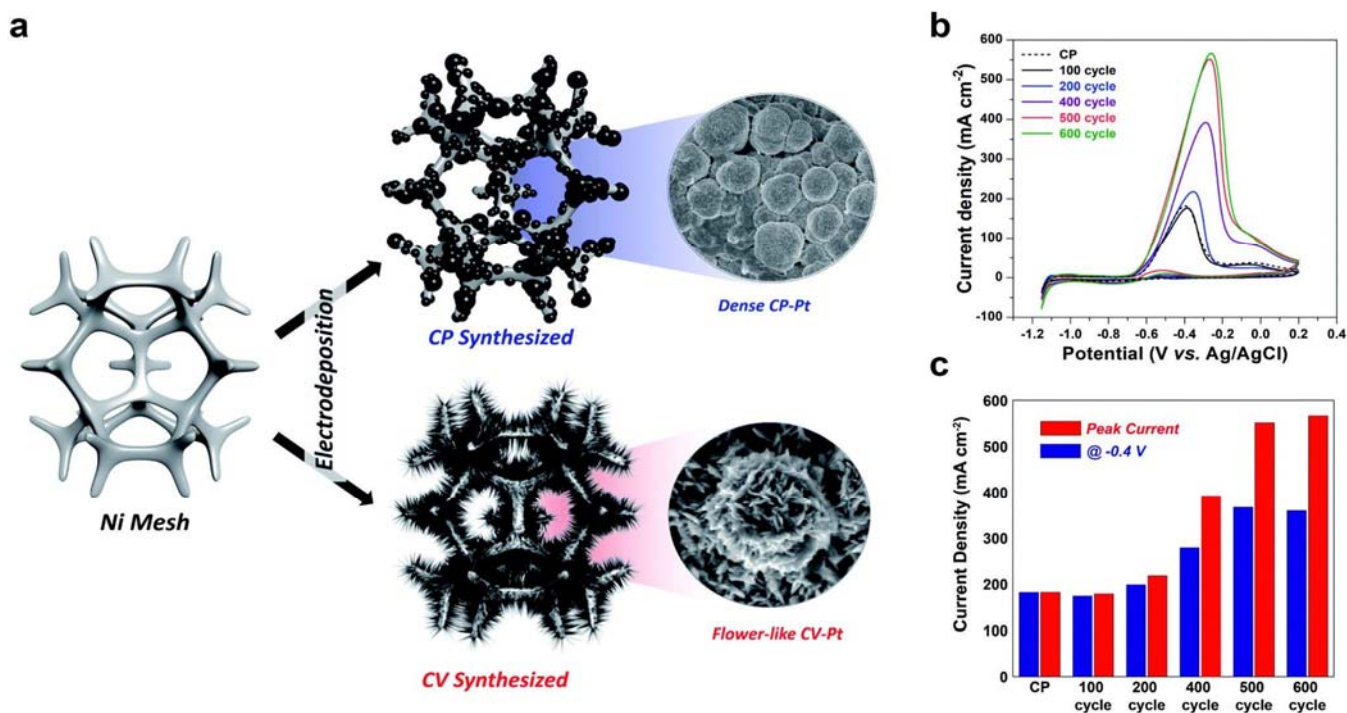


Figure 2. (a) Schematic illustration of the CP-Pt and CV-Pt electrodes. (b) CVs results and (c) Comparison of peak current density and current density at -0.4 V_{Ag/AgCl} for CV-Pts and CP-Pts. All electrocatalytic measurements were conducted with 1 M NH₃ in 5 M KOH. Reproduced with permission [42]. Copyright 2021, Royal Society of Chemistry.

To investigate the effect of morphology on AOR activity, the CV process was conducted with 1 M NH₃ in 5 M KOH. From Figure 2b, the current density began to increase at -0.65 V_{Ag/AgCl} representing AOR and exhibited a maximum current density around -0.3 V_{Ag/AgCl}; the current density then decreased due to strong adsorption of N_{ads}. The CV-Pt electrodes exhibited a higher peak current density than the CP-Pt electrodes; notably, the 600 CV-Pt electrode recorded a maximum current density of 560 mA cm⁻², which is three times higher than that of the CP-Pt electrode, as shown in Figure 2b,c. Since all electrodes have similar polycrystalline crystal structures and crystallinity of Pt as investigated using X-ray diffraction (XRD), it can be excluded the possibility of increasing the activity caused by a preferable crystal structure or facet for AOR. Instead, the major contribution to the increased current density is the enhanced active surface area for flower-shaped CV-Pt compared to unevenly dense structured CP-Pt. This work clearly reveals that the morphology, as well as the surface area of the electrocatalyst, is one of the critical factors affecting AOR performances.

W.B. Hu et al. prepared Pt particles with different morphology on indium tin oxide film (ITO) substrate by electrodeposition with controlling the current density from 0.2 mA cm⁻² to 1 mA cm⁻² [49]. With an increased current density, the Pt growth rate at the edge of the nucleus for Pt is faster than the rate at the other sites of the nucleus, resulting in a morphological change from spherical to flower-like.

To compare AOR activity between different electrodes, CVs were measured using Pt electrodes with spherical and flower-like morphologies with 0.1 M NH_3 in 1 M KOH. To prevent false evaluation due to irregular loading amounts of Pt on the electrode, the obtained CV data were normalized with the loaded catalyst amounts. The flower-like Pt particles exhibited a peak current density of $0.063 \text{ mA } \mu\text{g}^{-1}$, which is three times higher than that of the spherical Pt particle. It is mainly due to the difference in the surface area accompanied by each morphology. In fact, the flower-shaped Pt electrode exhibited two times higher electrochemical active surface area (ECSA) than the Pt spherical Pt electrode. Interestingly, when comparing AOR performance divided into ECSA of each Pt electrode, still, the flower-shaped Pt electrode showed advanced activity compared to spherical Pt. Besides the large surface area, the tips and sharp-edged flakes comprising flower morphology develop additional surface electric fields, affecting the enhancement of AOR kinetics.

Facet engineering is another important area to explore in terms of improving AOR kinetics. Yu Chen et al. synthesized Pt nanocubes (Pt-NCs) with dominant (100) facets using a facile hydrothermal method involving the agents of polyvinyl pyrrolidone (PVP), 2-methylimidazole, and ascorbic acid [50]. Each agent is critical in the preparation of the desired catalyst; for example, PVP served as the stabilizing agent, 2-methylimidazole was used as (100) facet-selective agent, and ascorbic acid was used to form nanocubes by controlling the reducing rate of Pt. The preferential (100) facet in the Pt-NCs was revealed by TEM images, as shown in Figure 3a,b.

The AOR activity of the Pt-NCs was evaluated using CV with 0.1 M NH_4OH in 1 M KOH and was compared with that of commercial Pt nanoparticles (Pt-NCs-JM) purchased from Johnson Matthey Corporation. In order to remove any possibility of affecting AOR coming from the different surface areas of Pt samples, the AOR activities were normalized using the collected ECSA value, as shown in Figure 3c. For both Pt samples, a remarkable peak indicating AOR starts at $0.5 V_{\text{RHE}}$ and the highest current density was observed at $0.7 V_{\text{RHE}}$. Pt-NCs exhibited a peak current density of $5.1 \text{ mA cm}_{\text{ECSA}}^{-2}$, whereas Pt-NCs-JM exhibited a peak current density of $2.6 \text{ mA cm}_{\text{ECSA}}^{-2}$. Given that Pt-NCs-JM comprises polycrystalline Pt, which has diverse Pt facets, it can be inferred that the advanced AOR performance in Pt-NCs is mainly due to the dominant Pt (100) facets in the sample.

Catalytic stability during electrolysis is another important factor in determining AOR performance. Generally, the strong adsorption of nitrogen atoms (N_{ads}) on Pt catalysts leads to active site deactivation, resulting in severe instability. The catalytic stability of the Pt electrodes was evaluated using constant potential electrolysis at $0.6 V_{\text{RHE}}$ with the same electrolyte conditions. From Figure 3d, the time-profiled current density over the mass of the loaded Pt catalysts (J-t) showed that Pt-NCs exhibited a higher initial current density and lower current density decay rate relative to Pt-NCs-JM. The Pt (100) facets are able to improve initial catalytic activity and stability for AOR by providing an appropriate binding strength for the intermediate.

Juan M. Feliu et al. also prepared (100) facet-dominant cubic platinum nanoparticles (Pt NPs) using the water-in-oil microemulsion method [51]. The Pt (100) facet fraction was adjusted by controlling the concentration of HCl added during synthesis. As the concentration of HCl is increased from 0% to 25%, the (100) fraction also increases from 10% to 44%; when the concentration of HCl is increased beyond 25%, the (100) fraction begins to decrease. To investigate how the (100) facet fraction affects AOR performance, CV was measured with 0.1 M NH_3 in 0.2 M NaOH. The Pt sample with a (100) facet fraction of 44% exhibited a current density six times higher than that of the sample with a (100) fraction of 10%. This work obviously suggested a way to increase desired Pt (100) fraction via adjusting the concentration of HCl agents and, furthermore, demonstrated the effect of the Pt (100) fraction on the AOR performance.

The promising effect of Pt (100) facet engineering was theoretically supported by density functional theory (DFT) studies [52,53]. Mavrikakis et al. compared the onset potential and activation barrier of Pt (100) to Pt (111) for each Gerischer-Mauerer and Oswin-

Salomon mechanism, as shown in Figure 3e [54]. For the Gerischer–Mauerer mechanism, on Pt (100), the PDS is the deprotonation of HNNH_{ads} to NNH_{ads} with the onset potential of 0.29 V, which is similar to that of 0.28 V on Pt (111). However, $\text{NH}_{2,\text{ads}}$ dimerization to N_2H_4 , has a higher barrier of 2.32 eV on Pt (100) than the activation barrier of 1.07 eV on Pt (111). It represents the ability of HNNH_{ads} deprotonation on Pt (100) is close to on Pt (111). However, N_2H_4 formation by $\text{NH}_{2,\text{ads}}$ dimerization on Pt (111) is more favorable than the dimerization on Pt (100). On the other hand, based on the Oswin–Salomon mechanism on Pt (100), the potential determining step (PDS) is the deprotonation of $\text{NH}_{2,\text{ads}}$ to NH_{ads} with the onset potential of 0.87 V, and the N_{ads} dimerization to N_2 has a low activation barrier of 0.53 eV. On the other hand, on Pt (111), the PDS (NH_{ads} to N_{ads}) has an onset potential of 0.52 V, which is lower than that of Pt (100), and the N_{ads} dimerization has a high activation barrier of 2.24 eV, which is much higher than that of Pt (100). It indicates that N_{ads} formation on Pt (100) is more difficult than the intermediate formation on Pt (111) referred by onset potentials. However, once N_{ads} formed, its dimerization and desorption on Pt (100) is more preferred than that on Pt (111) when comparing the activation barrier. Considering the theoretically calculated data, Pt (100) facet can provide the lowest activation barrier for N_2 formation following the Oswin–Salomon mechanism and also can explain experimental advances in Pt (100) engineering.

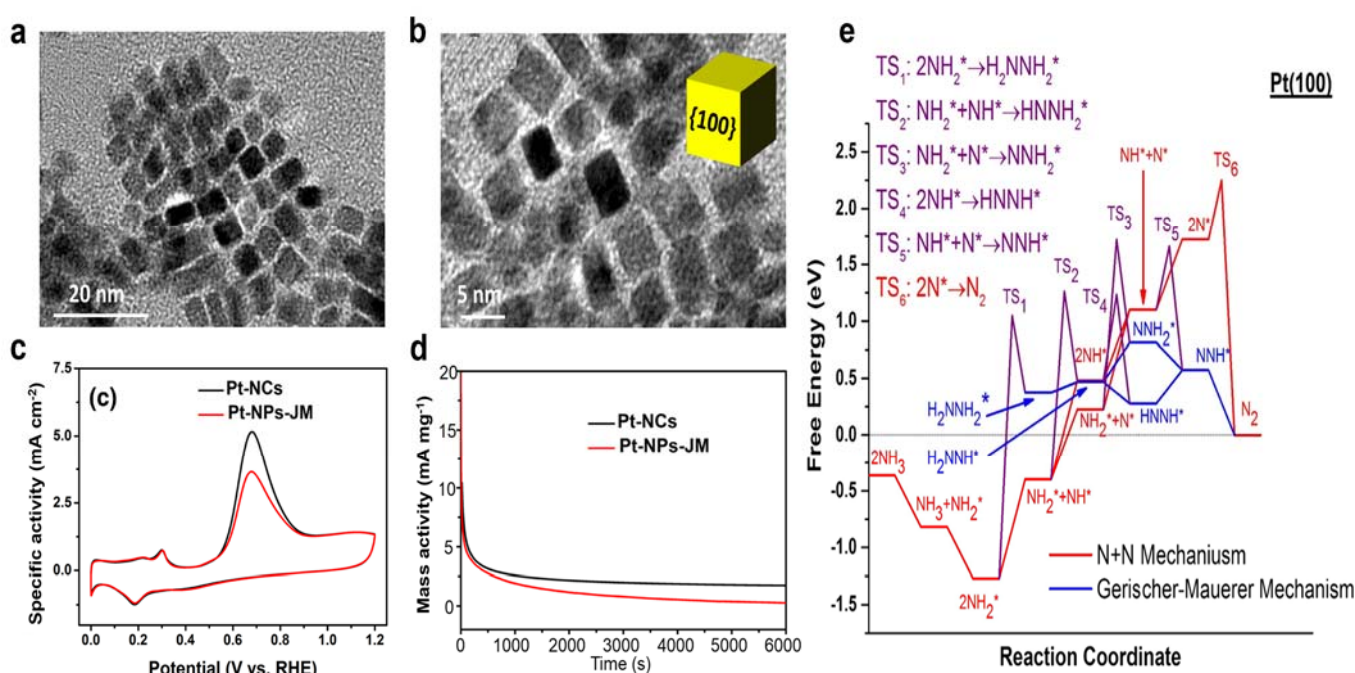


Figure 3. (a) The low and (b) the high magnified TEM images of Pt-NCs. (c) the CV curves normalized using the value of ESCA with a potential scan rate of 5 mV s^{-1} and (d) the time-profiled current density over the mass loaded on the electrode (J-t curves) at $0.6 \text{ V}_{\text{RHE}}$ for Pt-NCs and Pt-NPs-JM. All AOR performances were measured with $0.1 \text{ M NH}_4\text{OH}$ in 1 M KOH . Reproduced with permission [50]. Copyright 2020, Elsevier B. V. (e) Free-energy diagram for AOR on Pt (100) at 0.0 V . In purple are $\text{NH}_{x,\text{ads}}$ ($x = 0$ or 1 or 2) dimerization elementary steps with the respective transition-state (TS) energies. N + N mechanism indicates the Oswin–Salomon mechanism, and * indicates adsorption on the catalyst surface. Reproduced with permission [54]. Copyright 2021, Elsevier B. V.

3.1.2. Pt-Ir Bimetal Electrocatalysts

Pt is considered the most active AOR catalyst among noble metals. However, it should overcome the catalytic deactivation caused by the strong adsorption of N_{ads} ; this behavior is called surface poisoning. Pt-based binary and ternary catalysts with Ir, Ru, Rh, and Pd have been suggested to reduce surface poisoning and improve AOR performance [23,55–58].

Among these, Ir is the most representative candidate for Pt-based binary and ternary catalysts because it has a sufficient NH_3 dehydrogenation capacity and appropriately low N_{ads} affinity. For example, Pt-Ir bimetal catalysts can decrease potential onset relative to a single Pt catalyst and reduce surface poisoning by altering the electron state of Pt and weakening the adsorption strength for N_{ads} [59,60]. In this part, recent studies on Pt-Ir alloy synthesized in various ways and their origins for advancing AOR activity are discussed.

Minhua Shao et al. synthesized a catalyst by depositing Ir onto Pt (100) facets on carbon substrate (Ir-decorated Pt NCs/C) using the modified solvothermal method [59]. The uniform distribution of Ir on Pt was revealed by Energy-dispersive X-ray spectroscopy (EDS) mapping images in Figure 4a. The effect of Ir on Pt was evaluated by comparing LSVs between Ir-decorated Pt NCs/C and pure Pt NCs/C, in which current density was normalized using ECSA in the electrolyte of 0.1 M NH_3 in 0.1 M KOH. In Figure 4b, although both Ir-decorated Pt NCs/C and Pt/NCs exhibited pre-peaks at $0.30 V_{\text{RHE}}$, indicating NH_3 adsorption, the current density of Ir-decorated Pt NCs/C arose from a much lower onset potential of $0.43 V_{\text{RHE}}$ than that of Pt NCs/C started at $0.55 V_{\text{RHE}}$. Furthermore, the Ir-decorated Pt NCs/C exhibited a current density of 1.26 mA cm^{-2} , which was two times higher than that of Pt NCs/C; this confirms that Ir decorated on Pt results in not only reduced overpotential but also increased AOR kinetics.

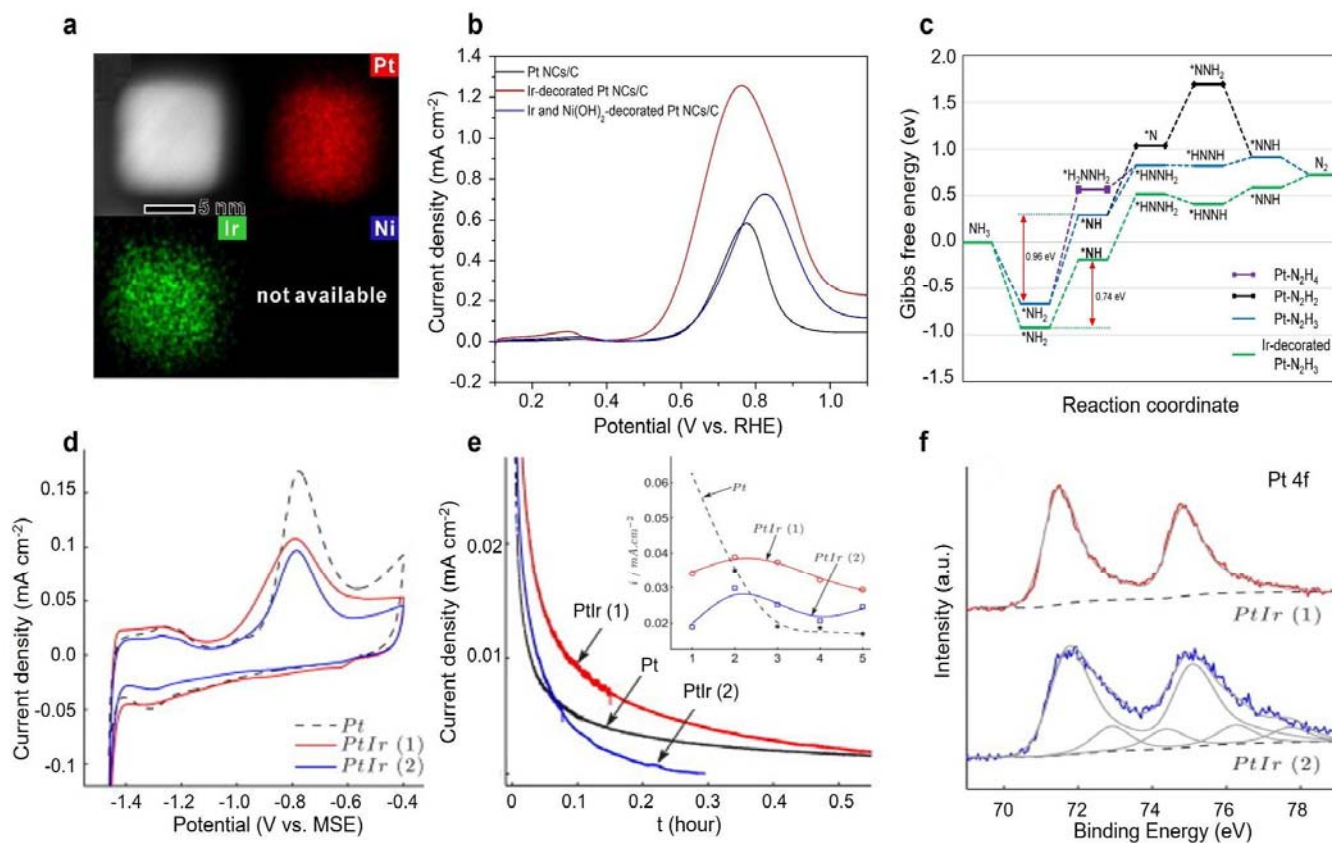


Figure 4. (a) HAADF-STEM images and corresponding EDS mapping images of Ir-decorated Pt NC. (b) the LSV curves were measured with 0.1 M NH_3 in 0.1 M KOH, where the current densities were normalized using the value of ECSA. (c) Gibbs free energy changes for each step of AOR pathways on Pt (100) and Ir-decorated Pt (100). Reproduced with permission [59]. Copyright 2020, Elsevier B. V. (d) The CV curves measured with 0.5 M NH_4OH in 1 M KOH, where current densities were normalized using the value of ECSA, (e) J-t curves at $-0.8 V_{\text{MSE}}$ of Pt, PtIr (1) and PtIr (2) and (f) Pt 4f XPS spectra for PtIr (1) and PtIr (2). Reproduced with permission [60]. Copyright 2013, Elsevier B. V.

Besides advancing in kinetic, catalytic stability was also improved by Ir decoration on Pt. The current density decay rates of the Ir-decorated Pt NCs/C and Pt NCs/C were

compared using constant potential electrolysis at $0.6 V_{RHE}$. The current density of the Ir-decorated Pt NCs/C decayed in 100 s, whereas that of the Pt NCs/C decayed immediately. Considering the major origin of instability observed for Pt electrocatalysts, it reveals that Ir decoration on Pt is effective in preventing Pt surface poisoning by storing N_{ads} .

To further investigate the role of Ir in this regard, the differences in Gibbs free energies of the Pt (100) and Ir-decorated Pt (100) were monitored using DFT calculations for each step of the AOR pathways, as shown in Figure 4c. The Ir-decorated Pt (100) exhibited a relatively low activation energy barrier of 0.74 eV for the dominant rate-determining step compared to pure Pt (100), which exhibited an energy barrier of 0.96 eV. From the experimental and theoretical investigations, it is found that the critical role of Ir on Pt is to improve reaction kinetics by lowering the energy barriers and to increase stability by preventing Pt poisoning.

Elena A. Baravona et al. synthesized Pt-Ir alloys using the polyol method under a pH of 7 (named PtIr (1)) and 8.5 (named PtIr (2)) [60]. As shown in Figure 4d, the AOR activity for both Pt-Ir alloys and the single Pt was evaluated using CV with 0.5 M NH_4OH in 1 M KOH, where the measured current densities were normalized using the value of ECSA of each sample. In terms of peak current density, PtIr (1) was less effective than pure Pt; however, PtIr (1) had a clear advantage in onset potential compared to pure Pt. PtIr (1) showed an onset potential for AOR at $-1.07 V_{MSE}$, which was 0.13 V less than that of the single Pt. The results indicate that the PtIr (1) alloy is better at facilitating high catalytic AOR activity in the low potential region than the single Pt.

Furthermore, the catalytic stabilities of Pt and PtIr (1) were evaluated using a time-profiled potential constant electrolysis at $-0.8 V_{MSE}$, as shown in Figure 4e. The PtIr (1) showed a higher initial current density and slower current density decay than that of the single Pt. These advances in terms of onset potential, the current density at low potential, and stability can mainly be attributed to the electronic effect between Pt and Ir atoms in the PtIr (1) alloy. Meanwhile, PtIr (2) exhibited an even worse AOR performance than pure Pt in terms of kinetics and stability; this is due to the formation of Pt oxide on the surface of the electrode during synthesis, unlike PtIr (1) and Pt which contain metallic Pt state. In the XPS spectra of Pt 4f, as shown in Figure 4f, PtIr (2) showed additional peaks at 72.9 eV and 74.4 eV, which corresponds to the oxidized Pt, while that of the metallic Pt is at 71.6 eV. The Pt oxide on PtIr (2) inhibited the adsorption of NH_3 , resulting in a high onset potential and low stability even as alloying Ir with Pt.

Pt-based ternary metal alloying is another promising strategy for advancing AOR performance. Particularly, the addition of a third transition metal onto Pt-Ir alloy has been mainly studied. Gan Wu et al. prepared a ternary PtIrNi alloy on supports comprising SiO_2 and CNT-COOH using the sonochemical-assisted method, as shown in Figure 5a [61]. The supports can provide a large surface area for the deposition of the three metals.

The AOR activities of various electrodes, including Pt/ SiO_2 -CNT-COOH, PtIr/ SiO_2 -CNT-COOH, and PtIrNi- SiO_2 -CNT-COOH, were compared using CVs with 0.1 M NH_3 in 1.0 M KOH; their current densities collected during CV were normalized by precious-group-metal (PGM) mass, as shown in Figure 5b. PtIrNi/ SiO_2 -CNT-COOH exhibited the lowest onset potential, followed by PtIr/ SiO_2 -CNT-COOH and Pt/ SiO_2 -CNT-COOH; this confirms that the presence of Ni in the alloy reduces the onset potential. For example, PtIrNi/ SiO_2 -CNT-COOH exhibited the lowest onset potential at $0.4 V_{RHE}$ and the highest current density of $124.0 A g^{-1}$. PtIr/ SiO_2 -CNT-COOH and Pt/ SiO_2 -CNT-COOH even recorded more positive values of onset potential, as much as $0.05 V_{RHE}$ and $0.15 V_{RHE}$, respectively, compared to that from PtIrNi/ SiO_2 -CNT-COOH. Moreover, the Ni ternary alloy exhibited the highest stability, which was measured at a constant $0.65 V_{RHE}$, among all Pt-based electrodes, as shown in Figure 5c.

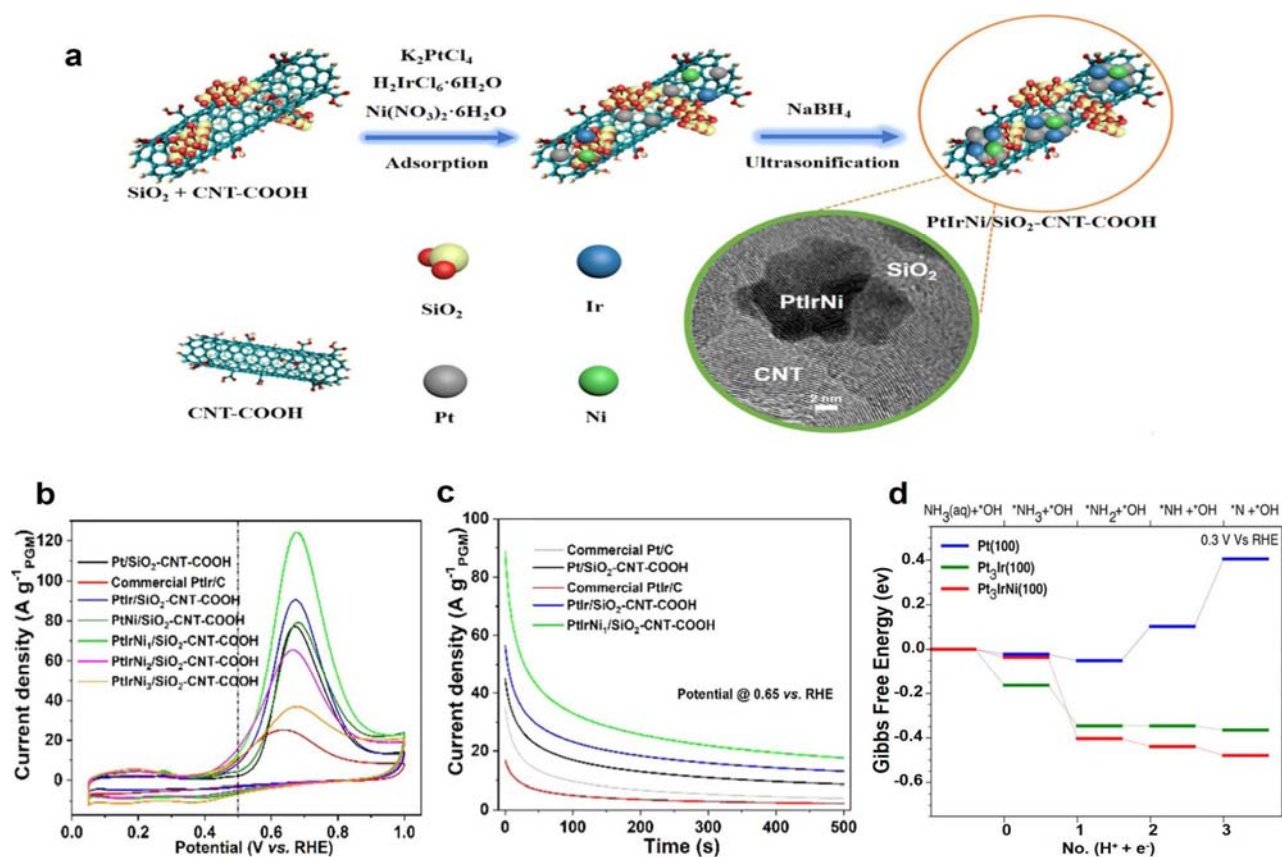


Figure 5. (a) Schematic illustration for the synthesis of PtIrNi/SiO₂-CNT-COOH. (b) the CV curves where current densities were normalized using precious-group-metal (PGM) mass and (c) the J-t curves at 0.65 V_{RHE} of Pt, PtIr, PtNi, PtIrNi₁, PtIrNi₂, PtIrNi₃ deposited on SiO₂-CNT-COOH, and commercial PtIr/C. The AOR performance was measured in Ar-saturated with 0.1 M NH₃ in 1.0 M KOH. (d) Free-energy diagram for elementary steps of NH₃ dehydrogenation on Pt (100) Pt₃Ir (100), Pt₃IrNi (100). Reproduced with permission [61]. Copyright 2020, American Chemical Society.

The enhancement of AOR performance by alloying with Pt, Ir and Ni was elucidated by DFT calculations. According to Gibbs's free energy changes for each elemental step of AOR, as shown in Figure 5d, the Pt-Ir alloy had a largely reduced thermodynamic barrier for dehydrogenation compared to the single Pt. Moreover, as alloying Ni with Pt-Ir, the barrier was further reduced significantly. By adding Ni to Pt-Ir alloy, d orbital states can be largely increased, resulting in facilitating NH₃ ads formation and adsorption, which is the major rate-determining step in the single Pt. This work demonstrated that a ternary metal alloy is a promising approach to preparing electrocatalysts for AOR in terms of onset potential and stability. However, even if AOR performance has been largely developed by multi-modification using Pt, for example, morphology control, facet engineering, alloy, and so on, the high cost of Pt and Pt-based electrodes remain a significant challenge for advancing AOR in practice. Therefore, the rational design of electrocatalysts comprising non-precious elements is highly required. We summarized the AOR performance on Pt-based catalysts in Table 1.

Table 1. A brief summary of experimental studies on AOR using various Pt-based electrocatalysts.

	Catalysts	Electrolyte	Onset Potential (V _{RHE})	Peak Current Density	Ref
Pt-based catalysts	500 CV-Pt	1 M NH ₃ + 5 M KOH	0.42	0.27 mA cm _{ECSA} ⁻²	[42]
	Flower-like Pt	0.1 M NH ₃ + 1 M KOH	0.5	0.48 mA cm _{ECSA} ⁻²	[49]
	Pt nanocubes (Pt-NCs)	0.1 M NH ₄ OH + 1 M KOH	0.5	5.1 mA cm _{ECSA} ⁻²	[50]
	Pt nanoparticles (Pt NPs)	0.1 M NH ₃ + 0.2 M NaOH	0.55	1.96 mA cm _{ECSA} ⁻²	[51]
	Ir-decorated Pt	0.1 M NH ₃ + 0.1 M KOH	0.43	1.26 mA cm _{ECSA} ⁻²	[59]
	PtIr nanoparticle	0.5 M NH ₄ OH + 1 M KOH	0.4	0.11 mA cm _{ECSA} ⁻²	[60]
	PtIrNi/SiO ₂ -CNT-COOH	0.1 M NH ₃ + 1 M KOH	0.4	2.48 mA cm ⁻²	[61]
	PtNC/C	0.1 M NH ₃ + 1 M KOH	0.48	3.89 mA cm _{ECSA} ⁻²	[48]
	Pt nanosheet	0.1 M NH ₃ + 1 M KOH	0.57	0.32 mA cm _{ECSA} ⁻²	[62]
	Pt thin film	0.1 M NH ₃ + 0.2 M NaOH	0.5	0.212 mA cm _{ECSA} ⁻²	[63]
	Pt nanofilm	0.1 M NH ₃ + 1 M KOH	0.45	2.15 mA cm ⁻²	[1]
	C-Pt/SnO ₂	0.1 M NH ₃ + 1 M KOH	0.45	1.6 mA cm ⁻²	[64]
	Pt/PBI/MWNT-CeO ₂	0.1 M NH ₃ + 1 M KOH	0.45	0.26 mA cm _{ECSA} ⁻²	[65]
	Pt/C-ITO	1 M NH ₄ OH + 1 M KOH	0.54	1.35 mA cm _{ECSA} ⁻²	[66]
	Y ₂ O ₃ -modified Pt/Si	0.1 M NH ₃ + 1 M KOH	0.45	0.19 mA cm _{ECSA} ⁻²	[21]
	Pt/NGA	0.1 M NH ₃ + 1 M KOH	0.5	0.64 mA cm _{ECSA} ⁻²	[67]
	Pt ₉₀ Ir ₁₀	0.1 M NH ₃ + 1 M KOH	0.58	0.37 mA cm ⁻²	[68]
	Pt-Ir nanocubes	0.1 M NH ₃ + 1 M KOH	0.45	1.32 mA cm ⁻² ECSA	[69]
	Pt/Ir/MWCNT	0.1 M NH ₃ + 0.1 M KOH	0.38	0.23 mA cm ⁻² ECSA	[70]
	PtIrZn	0.1 M NH ₃ + 0.5 M NaOH	0.3	0.56 mA cm ⁻²	[71]
	PtIrCu HCOND	0.1 M NH ₃ + 1 M KOH	0.35	122.9 A g ⁻¹ Pt	[72]
	PtIrZn ₂ /CeO ₂ -ZIF-8	0.1 M NH ₃ + 1 M KOH	0.35	0.64 mA cm ⁻²	[73]
	Pt ₉₀ Ru ₁₀ /C	1 M NH ₄ OH + 1 M KOH	0.5	0.91 mA cm _{ECSA} ⁻²	[74]
	Pt ₆ Ru-NCs	0.1 M NH ₃ + 1 M KOH	0.5	1.02 mA cm _{ECSA} ⁻²	[75]
Pt ₈₅ Pd ₁₅ /rGO	0.1 M NH ₃ + 1 M KOH	0.47	1.46 mA cm ⁻²	[57]	

3.2. Ni-Based Metal Electrocatalysts

Pt and Pt-based noble metals have been considered active catalysts in AOR because of their low overpotential and high N₂ selectivity; however, their high cost and susceptibility to deactivation have proven to be significant challenges. Recently, non-noble metal-based electrocatalysts have been proposed as an alternative to Pt-based electrocatalysts [76–78].

Ni has been studied as a potential catalyst to replace noble metals because it is intrinsically satisfactory for adsorbed NH_3 dehydrogenation and $\text{NH}_{x,\text{ads}}$ dimerization and shows experimental activity in AOR with its abundance [20,40,76]. Notably, Ni exhibited significantly promising long-term stability for a few hours, while Pt-based catalysts were deactivated within a few seconds. However, formation of by-products, N_2H_4 , NO_2^- , NO_3^- , and so on, leads to decrease selectivity for N_2 production [79]. To overcome the limitation and further improve AOR activity, Ni-based binary and ternary catalysts have been studied [80–82]. This section focuses on recent research regarding combinations of Ni with hetero-atoms and their effects on AOR.

Ni alloying with Cu elements has been widely proposed to promote AOR performance by overcoming the challenges of imperfect reaction rate and N_2 selectivity [19].

Shanwen Tao et al. synthesized Ni-Cu layered hydroxides ($\text{Ni}_{0.8}\text{Cu}_{0.2}$ LHs) on carbon fiber cloth using the hydrothermal method, followed by electrochemical activation over 200 CV cycles in the potential range of $-0.2 \text{ V}_{\text{Ag}/\text{AgCl}}$ to $1.0 \text{ V}_{\text{Ag}/\text{AgCl}}$, as shown in Figure 6a [24]. The AOR performance of $\text{Ni}_{0.8}\text{Cu}_{0.2}$ LHs was evaluated using CV with $55 \text{ mM NH}_4\text{Cl}$ in 0.5 M NaOH and compared with that of bare $\text{Ni}(\text{OH})_2$. In Figure 6b, both electrodes exhibited an increase in the current density at $0.43 \text{ V}_{\text{Ag}/\text{AgCl}}$, indicating the oxidation from hydroxide to oxyhydroxide, such as the transformation of $\text{Ni}_{0.8}\text{Cu}_{0.2}\text{OOH}$ from $\text{Ni}_{0.8}\text{Cu}_{0.2}$ LHs ($\text{Ni}_{0.8}\text{Cu}_{0.2}(\text{OH})_2$) and NiOOH from $\text{Ni}(\text{OH})_2$, respectively. In the potential over $0.43 \text{ V}_{\text{Ag}/\text{AgCl}}$ representing the AOR region, $\text{Ni}_{0.8}\text{Cu}_{0.2}$ LHs showed a rapid increase, and it represents a higher current density than that from $\text{Ni}(\text{OH})_2$. Additionally, the Tafel slope of $\text{Ni}_{0.8}\text{Cu}_{0.2}$ LHs was much smaller than that of $\text{Ni}(\text{OH})_2$, indicating the electron transfer within $\text{Ni}_{0.8}\text{Cu}_{0.2}$ LHs is relatively fast, as shown in Figure 6c. From this, it can be posited that the addition of Cu to the Ni oxyhydroxide improved both electron transfer and AOR kinetics. The first origin of AOR enhancement for $\text{Ni}_{0.8}\text{Cu}_{0.2}$ LHs is a large surface area compared to $\text{Ni}(\text{OH})_2$. Moreover, the adjusted strength of NH_3 adsorption promotes the formation of the first intermediate of the $\text{Ni}_{1-x}\text{Cu}_x\text{OOH}(\text{NH}_3)_{\text{ads}}$.

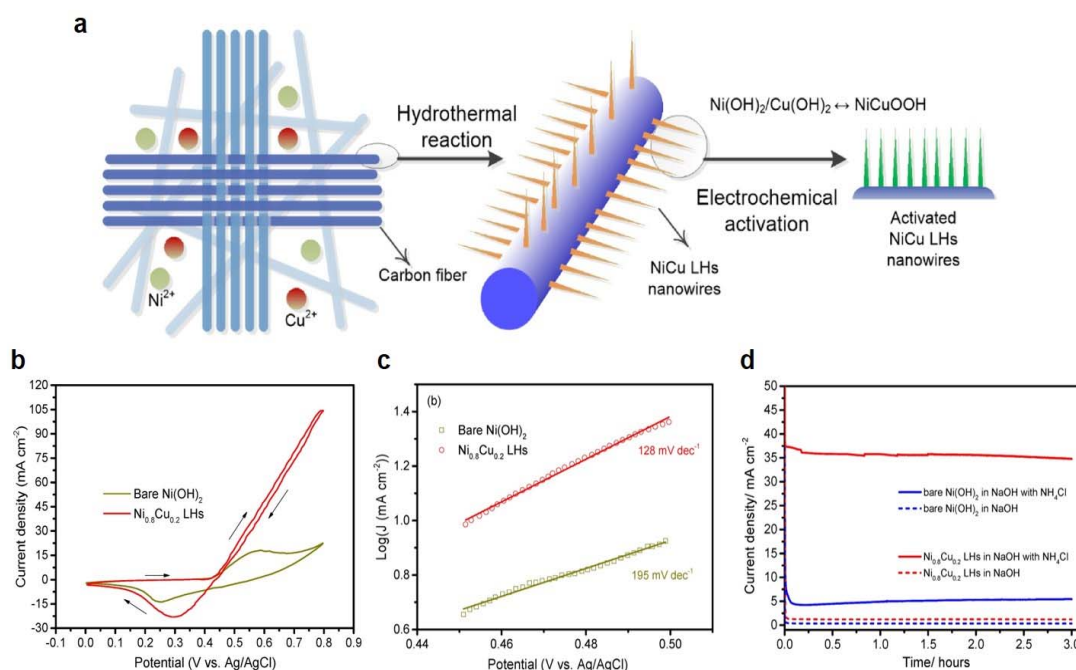


Figure 6. (a) Schematic illustration for the preparation of $\text{Ni}_{0.8}\text{Cu}_{0.2}$ LHs on carbon fiber cloth substrate, (b) the CVs and (c) the Tafel plots for $\text{Ni}_{0.8}\text{Cu}_{0.2}$ LHs and bare $\text{Ni}(\text{OH})_2$. (d) the J-t curves at $0.55 \text{ V}_{\text{Ag}/\text{AgCl}}$. The AOR performance was measured with $55 \text{ mM NH}_4\text{Cl}$ in 0.5 M NaOH . Reproduced with permission [24]. Copyright 2017, Elsevier B. V.

Furthermore, the catalytic stability of $\text{Ni}_{0.8}\text{Cu}_{0.2}$ LHs was evaluated using constant potential electrolysis of $0.55 \text{ V}_{\text{Ag}/\text{AgCl}}$ under the same electrolytic conditions discussed above. As shown in Figure 6d, the addition of NH_4Cl resulted in an increase in current density for both $\text{Ni}_{0.8}\text{Cu}_{0.2}$ LHs and bare $\text{Ni}(\text{OH})_2$ electrodes. Interestingly, $\text{Ni}_{0.8}\text{Cu}_{0.2}$ LHs showed a stable current density of 35 mA cm^{-2} , which was approximately seven times higher than that of bare $\text{Ni}(\text{OH})_2$ for at least 3 h. The NH_3 removal efficiency, determined at $0.55 \text{ V}_{\text{Ag}/\text{AgCl}}$, reached 84%, whereas bare $\text{Ni}(\text{OH})_2$ recorded an NH_3 removal efficiency of 58%. Based on all the results discussed above, the Cu-doped Ni LDH was able to enhance AOR performance in terms of activity, stability, and ultimate NH_3 removal efficiency.

Masaharu Nakayama et al. prepared Ni^{2+} and Cu^{2+} co-intercalated electrocatalysts on layered MnO_2 (NiCu/MnO_2) using a two-step synthetic process: the electrodeposition of tetrabutylammonium cations (TBA^+)/ MnO_2 at a constant potential of $1.0 \text{ V}_{\text{Ag}/\text{AgCl}}$ and then the ion exchange reaction, carried out by immersing the catalyst in a solution containing Ni^{2+} and Cu^{2+} [26]. As shown in Figure 7a, TBA/MnO_2 showed a peak at 7.14° , which represents a (001) plane of layered MnO_2 and a d-spacing of 1.23 nm. On the other hand, in NiCu/MnO_2 , the peak of the (001) plane split and appeared at 10° and 12° , and the d-spacing decreased to 0.88 nm and 0.75 nm. The reduced d-spacing indicates that the bulky TBA^+ ions were exchanged into Ni^{2+} and Cu^{2+} ions. Additionally, uniformly electrodeposited surface was identified through the SEM images as shown in Figure 7b,c.

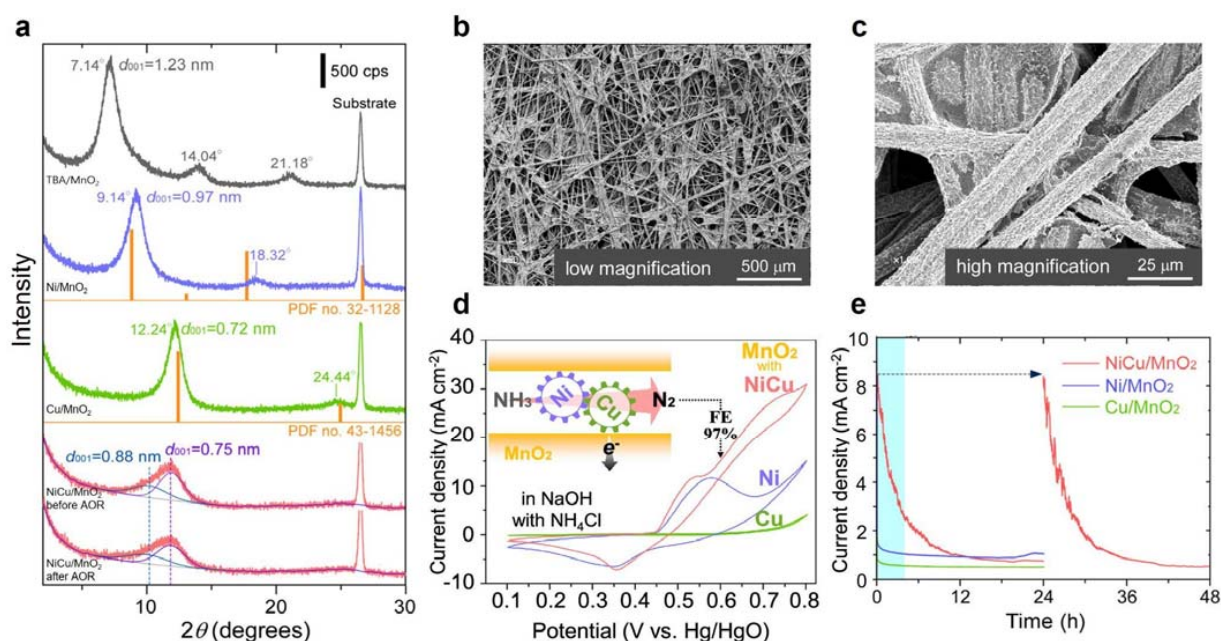


Figure 7. (a) The XRD patterns of TBA/MnO_2 (black line), Ni/MnO_2 (blue line), Cu/MnO_2 (green line), NiCu/MnO_2 before AOR (upper red line) and NiCu/MnO_2 after AOR (lower red line). (b) The low and (c) the high-magnified SEM images of NiCu/MnO_2 deposited on carbon paper. (d) The CV curves and (e) the J-t curves at $0.6 \text{ V}_{\text{Hg}/\text{HgO}}$ for NiCu/MnO_2 , Ni/MnO_2 , and Cu/MnO_2 . The AOR performance was measured with 55 mM NH_4Cl in 0.5 M NaOH. Reproduced with permission [26]. Copyright 2021, American Chemical Society.

The electrocatalytic AOR performance for NiCu/MnO_2 was evaluated using CV with 55 mM NH_4Cl in 0.5 M NaOH, as shown in Figure 7d. NiCu/MnO_2 exhibited a peak at $0.53 \text{ V}_{\text{Hg}/\text{HgO}}$, confirming the oxidation from Ni^{2+} to Ni^{3+} , which was followed by a rapid increase in current density, an indication of facile AOR. Although Ni/MnO_2 also exhibited two distinct increases in current density, attributing to Ni^{2+} oxidation at $0.65 \text{ V}_{\text{Hg}/\text{HgO}}$ and AOR, the subsequent increase in current density was much lower than that of NiCu/MnO_2 . These results obviously represented that the addition of Cu^{2+} into Ni^{2+} intercalated MnO_2 reduced the onset potential for Ni^{2+} oxidation and increased the current density for AOR.

Moreover, the NiCu/MnO₂ showed promising catalytic stability during constant potential electrolysis at 0.6 V_{Hg/HgO} for 24 h, as shown in Figure 7e. Even if the current density steadily decreased as time passed, the current density was recovered in the 2nd-run, in a re-prepared fresh electrolyte after 24 h. This indicates that the current density decay was not originated from deactivation or electrode corrosion but from the rapid consumption of NH₃ at the NiCu/MnO₂ electrode. In addition, using online gas chromatography, the desired N₂ product selectivity was estimated to be 97.4%. This work revealed that the addition of Cu²⁺ in Ni²⁺ intercalated in MnO₂ could enhance AOR performance by mediating the electron transfer between Ni²⁺ and NH₃ and facilitating the oxidation of adsorbed NH₃.

Lately, to further develop AOR performance, researchers have suggested adding the third hetero-metal to Ni-Cu-based electrocatalysts. Junmin Xue et al. synthesized triple Ni-Cu-Fe oxyhydroxides onto carbon paper (NiCuFe electrode) using electrodeposition at a constant potential of −1.15 V_{Hg/Hg2Cl2}, followed by electrochemical activation [27]. The AOR activity of the NiCuFe electrode was evaluated using CV with 55 mM NH₄Cl in 0.5 M NaOH and compared with that of the NiCu electrode. The NiCuFe electrode exhibited a rapid increase in current density over 0.36 V_{Hg/Hg2Cl2}, and its current density reached 60 mA cm^{−2} at 0.7 V_{Hg/Hg2Cl2}, whereas the current density of the NiCu electrode also increased over 0.45 V_{Hg/Hg2Cl2} and its current density only reached 30 mA cm^{−2} at 0.7 V_{Hg/Hg2Cl2}. This shows that the addition of Fe to NiCu significantly reduced the onset potential for AOR and increased the current density generated by AOR. Moreover, in the stability test during the constant potential electrolysis at 0.55 V_{Hg/Hg2Cl2}, the NiCuFe electrode exhibited an initial current density of 40 mA cm^{−2}, which was two times higher than that of the NiCu electrode. The current density decreased as NH₃ was consumed. The NiCuFe electrode recorded a high NH₃ removal efficiency of 95 % quantified using the indophenol method, and a selective NH₃ conversion to N₂ also occurred, with a minor product of NO₃[−].

The effect of doping Fe into NiCu electrode on AOR activity was additionally revealed using DFT calculation. According to DFT calculation, the first step of the reaction, the adsorption of NH₃ on an oxygen atom bonded to Ni and the NiCu electrode, showed the highest energy barrier of 4.91 eV among the tailored elementary steps. The addition of Fe, which has relatively low electronegativity, to the NiCu electrode, resulted in a significant increase in electron density around oxygen atoms and lowered the energy barrier to 1.08 eV. This suggests that Ni-Cu alloys doped with low electronegative elements, such as Fe, are able to accelerate the adsorption of NH₃ and ultimately improve AOR kinetics.

Besides Ni and Cu combination, diverse mixture of hetero-atoms and each element's effects have been experimentally proposed for AOR. Jianhui Wang et al. prepared physically mixed Ag and Ni electrocatalysts (Ag/Ni) by facile hand-mixing method [83]. The Ag/Ni was measured AOR performances by CV with 0.5 M NH₃ in 1.5 M NaOH and compared its activity with pristine Ag and Ni, respectively. The pristine Ag represented no catalytic activity in the potential region of CVs, whereas the pristine Ni exhibited a current density increase from 0.6 V_{Hg/HgO}. However, its dominant product from electrolysis was not N₂ but O₂, indicating OER is dominant rather than AOR on the electrode having Ni alone. On the other hand, the Ag/Ni showed a significant current density increase from lower onset potential at 0.46 V_{Hg/HgO}, which is a much higher current density than pristine Ni. Furthermore, Ag/Ni produced N₂ as a major product, representing its superior activity for AOR. The faradaic efficiency for N₂ production was recorded at 59.8%, while constant potential electrolysis at 0.7 V_{Hg/HgO} for 2 h. Furthermore, from the control experiments of CVs with and without NH₃, as shown in Figure 8a, the synergistic effect of Ag and Ni for AOR was discussed. As anodic scanning with NH₃, the peak for Ag⁺ oxidation to Ag²⁺, typically observed during the scan without NH₃, disappeared and which indicates the oxidized Ag⁺ can form a strong Ag⁺-NH₃ complex, suppressing further NH₃ oxidation. On the other hand, pristine Ni exhibited similar CV results regardless of NH₃ presence in the solution because the competitive reaction of OER was more favorable than AOR on

the Ni-only surface. Interestingly, Ag/Ni facilitated each $\text{Ag}^+ \text{-NH}_3$ complex formation and OH^- adsorption on Ni, and finally, they synergistically promoted to produce N_2 by applying potentials over $0.4 \text{ V}_{\text{Hg}/\text{HgO}}$, as shown in Figure 8b.

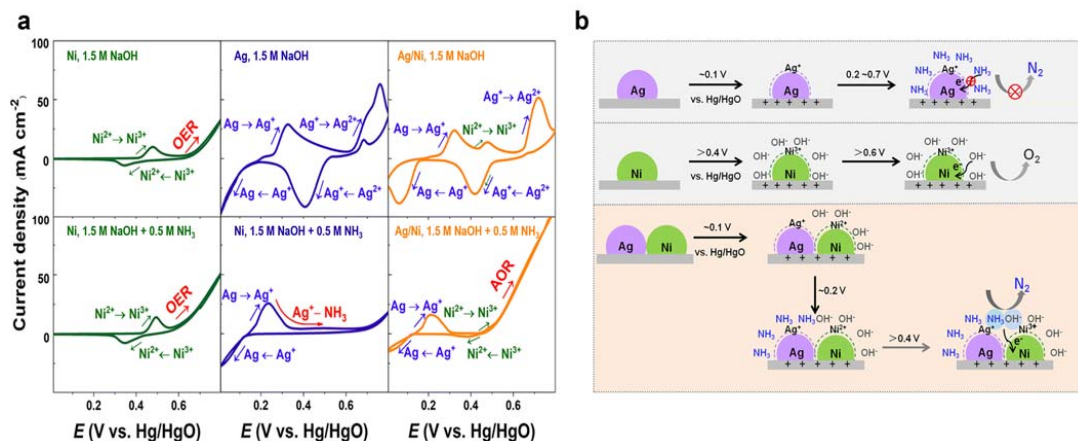


Figure 8. (a) The CV curves of Ni, Ag and Ag/Ni on the glassy carbon electrode. The AOR performance was measured with and without 0.5 M NH₃ in 1.5 M NaOH. (b) Schematic mechanism of Ag and Ni in the AOR. Reproduced with permission [83]. Copyright 2022, Royal Society of Chemistry.

The studies for developing AOR using Pt and Ni-based electrocatalysts have been mainly reported, whereas the research using other elemental compositions has been rarely studied. Furthermore, although new groups of catalysts, for example, CuO, CuSn(OH)₆, TiO and so on, were suggested, their AOR performances still need to be advanced [77,84,85]. Their recorded AOR activities are summarized in Table 2. It is highly required not only to search for new latent electrocatalyst candidates but also to advance their AOR performance using effective strategies.

Table 2. A brief summary of experimental studies on AOR using various non-noble metal electrocatalysts.

	Catalysts	Electrolyte	Onset Potential (V _{RHE})	Stability	N ₂ Selectivity (%)	Removal Efficiency (%)	Ref
Ni-based catalysts	Ni _{0.8} Cu _{0.2} LHs	0.55 M NH ₄ Cl + 0.5 M NaOH	1.39	35 mA cm ⁻² for 3 h	-	84	[24]
	NiCu/MnO ₂	0.055 M NH ₄ Cl + 0.5 M NaOH	1.6	3 mA cm ⁻² for 4 h	97.4	-	[26]
	NiCuFe	0.055 M NH ₄ Cl + 0.5 M NaOH	1.43	20 mA cm ⁻² for 12 h	-	89.4	[27]
	Ag/Ni	0.5 M NH ₃ + 1.5 M NaOH	1.37	10 mA cm ⁻² for 350 h	59.8	-	[83]
	NiCu/CP	0.055 M NH ₄ Cl + 0.5 M NaOH	1.47	8 mA cm ⁻² for 2 h	-	78	[19]
	Wire-in-plate nanostructured Ni(OH) ₂ -Cu ₂ O@CuO	1 M NH ₃ + 1 M KOH	1.37	60 mA cm ⁻² for 32 h	-	-	[86]
	NiCu DHTs	0.05 M NH ₄ OH + 0.1 M NaOH	1.31	0.5 mA cm ⁻² for 1 h	-	-	[87]
	NiCu/BDD	0.5 M NH ₃ + 0.5 M NaOH	1.35	5 mA cm ⁻² for 7 h	88.6	44.8	[88]
Cu-based catalysts	NiCuCo-S-T/CP	0.2 M NH ₄ Cl + 1 M NaOH	1.24	105 mA cm ⁻² for 12 h	81.2	98	[89]
	NiO-TiO ₂	0.2 M NH ₄ NO ₃ + 1 M NaOH	1.53	-	90	96.4	[90]
	CuO	1 M NH ₃ + 1 M KOH	1.19	200 mA cm ⁻² for 400 h	62.8	-	[84]
	CuSn(OH) ₆	10 mM NH ₃ + 0.5 M K ₂ SO ₄	1.56	-	84.5	-	[85]
Ti-based catalyst	TiO	0.1 M NH ₃ + 0.5 M NaOH	0.4	0.01 mA cm ⁻² for 2 h	-	-	[77]

4. Summary and Perspective

NH₃ has been gaining attention as a sustainable fuel and a carbon-free hydrogen carrier with a high energy density and high hydrogen content. Given this, the electrochemical NH₃ oxidation (AOR) is a key reaction for generating electricity in NH₃ fuel cells and producing H₂ fuel in NH₃ electrolyzers. However, the sluggish kinetics of AOR give rise to severe drawbacks of overpotential and reaction rate, even though it is thermodynamically favorable. These experimental challenges have been overcome by developing modified electrocatalysts, as reviewed in this work.

Pt electrocatalysts have been considered for use in AOR due to their superior NH₃ affinity and rapid AOR kinetics; because of this, Pt electrocatalysts have been further studied by exploring the diverse strategies modifying morphology and exposure facet on the surface, alloying, and so on. Particularly, a Pt-Ir was able to significantly improve the reaction kinetics of AOR by effectively reducing the energy barrier. Meanwhile, recently, cost-effective non-noble metal catalysts, especially Ni-based catalysts, have also been intensively suggested as alternatives to Pt. In particular, Ni-Cu bimetal catalysts exhibited the most promising AOR performance in terms of reaction rate and stability by adjusting the affinity of NH₃ and intermediates on Ni and Cu.

However, still searching for robust new catalysts and their development is necessary in order to perform AOR in practice. Especially to develop cost-effective non-noble metal-based electrocatalysts for AOR, several challenges need to be overcome. First, selective AOR in low overpotential regions is important. However, typical non-noble metal-based electrocatalysts exhibited AOR performance in high overpotential, and thus, the AOR competes with competitive reactions, such as water oxidation or NH₃ oxidation to NO₃⁻ or NO₂⁻, and so on. However, it was found that forming alloys with hetero-atoms can alter the electronic structure of catalysts resulting in reducing the NH₃ adsorption energy barrier and effectively reducing the overpotential [27,61,89].

Another important factor is AOR rate, which can be determined by current density. Doping or alloying can also be effective in increasing the current density by stabilizing reaction intermediates and enhancing reaction kinetics. In addition, the engineering morphology of electrocatalysts can be a key suggestion to facilitate reactions. The nano-sized electrocatalyst provides lots of active catalytic sites in large surface areas, leading to advanced current densities for AOR. Moreover, combining electrocatalysts with conductive supports or substrates comprising electrodes can promote significantly improved AOR performance. Substrates, such as carbon paper, carbon nanotube (CNT), Ni foam, and so on, have large surface areas and high intrinsic conductivities, reducing electron transfer resistance within the electrocatalysts coupled with the substrates and improving the AOR activity [61,88,91].

Unlike catalyst modifications, it has been rarely studied evaluating the total performance, including AOR and the counter reduction reaction in single-cell and engineering environmental conditions. For example, in order to effectively produce energy from NH₃ fuel or to extract H₂ from NH₃ electrolysis in practice, it is necessary to construct a single-cell typed real device composed of the developed catalysts and evaluate performance using the device. To our knowledge, the best faradaic efficiency of N₂ and H₂ production was 90% and 90%, respectively, from NH₃ during current density constant electrolysis at 200 mA cm⁻², where the potential difference of 0.85 V was measured in the single-cell composed with two Pt electrodes [42]. In addition, the total performance can be improved by optimizing reaction environmental conditions. For instance, the reaction operating temperature can be a critical factor directly affecting to the reaction rate [16,92–95]. As referring to the previous work, the device's current density was largely increased to 250 mA cm⁻² at 60 °C compared to the current density of 80 mA cm⁻² measured at room temperature. Therefore, to use NH₃ as a promising energy source efficiently, it is highly necessary to engineer and optimize device set-up and operating conditions.

Besides developing catalysts, a fundamental understanding of the reaction mechanism is critical to further improve AOR. Currently, the AOR mechanism has been mainly investi-

gated as suitable for Pt catalysts. However, actual reaction mechanisms or rate-determining steps can be different depending on the types of electrocatalysts. The DFT calculations have been widely applied to propose reaction mechanisms and elucidate the key effect for the catalytic modification [20,96,97]. With advances in theoretical investigation, observations of reaction mechanisms experimentally are important by monitoring adsorbed intermediates. Recently, efforts to investigate actual reaction mechanisms on electrocatalysts have been reported using in-situ or operando characterizations [1,21,98]. Considering the progress, the AOR has significant potential to develop as practically by combining catalytic modification and device engineering and fundamental studies.

Author Contributions: Conceptualization and writing—original draft preparation by J.H.J. and S.Y.P., writing review and editing, and supervision by D.H.Y. and Y.J.J. Funding acquisition by Y.J.J. All authors have read and agreed to the published version of the manuscript.

Funding: This work was supported by the Korea Institute of Energy Technology Evaluation and Planning (KETEP) grant funded by the Korea government (MOTIE) (No. 20224000000440, Sector coupling energy industry advancement manpower training program), and the Korea Institute of Energy Technology Evaluation and Planning (KETEP) grant funded by the Ministry of Trade, Industry & Energy (MOTIE) (No. 20223030030090).

Data Availability Statement: The datasets used and analyzed during the current study are available from the corresponding references listed.

Conflicts of Interest: The authors declare no conflict of interest.

References

1. Matsui, T.; Suzuki, S.; Katayama, Y.; Yamauchi, K.; Okanishi, T.; Muroyama, H.; Eguchi, K. In Situ Attenuated Total Reflection Infrared Spectroscopy on Electrochemical Ammonia Oxidation over Pt Electrode in Alkaline Aqueous Solutions. *Langmuir* **2015**, *31*, 11717–11723. [[CrossRef](#)] [[PubMed](#)]
2. Kim, H.; Yang, W.; Lee, W.H.; Han, M.H.; Moon, J.; Jeon, C.; Kim, D.; Ji, S.G.; Chae, K.H.; Lee, K.-S.; et al. Operando Stability of Platinum Electrocatalysts in Ammonia Oxidation Reactions. *ACS Catal.* **2020**, *10*, 11674–11684. [[CrossRef](#)]
3. Lamb, K.E.; Dolan, M.D.; Kennedy, D.F. Ammonia for hydrogen storage; A review of catalytic ammonia decomposition and hydrogen separation and purification. *Int. J. Hydrogen Energy* **2019**, *44*, 3580–3593. [[CrossRef](#)]
4. Lumley, M.A.; Radmilovic, A.; Jang, Y.J.; Lindberg, A.E.; Choi, K.S. Perspectives on the Development of Oxide-Based Photocathodes for Solar Fuel Production. *J. Am. Chem. Soc.* **2019**, *141*, 18358–18369. [[CrossRef](#)]
5. Jang, Y.J.; Choi, K.-S. Enabling electrochemical N₂ reduction to NH₃ in the low overpotential region using non-noble metal Bi electrodes via surface composition modification. *J. Mater. Chem. A* **2020**, *8*, 13842–13851. [[CrossRef](#)]
6. Choe, S.; Kim, S.M.; Lee, Y.; Seok, J.; Jung, J.; Lee, J.S.; Jang, Y.J. Rational design of photocatalysts for ammonia production from water and nitrogen gas. *Nano Converg.* **2021**, *8*, 22. [[CrossRef](#)] [[PubMed](#)]
7. Jang, Y.J.; Evans, T.A.; Samanta, B.; Zeng, K.; Toroker, M.C.; Choi, K.-S. A comparative study of Bi, Sb, and BiSb for electrochemical nitrogen reduction leading to a new catalyst design strategy. *J. Mater. Chem. A* **2021**, *9*, 20453–20465. [[CrossRef](#)]
8. Lee, C.; Kim, H.; Jang, Y.J. Three Phase Boundary Engineering Using Hydrophilic–Hydrophobic Poly(N-isopropylacrylamide) with Oxygen-Vacant TiO₂ Photocatalysts for Photocatalytic N₂ Reduction. *ACS Appl. Energy Mater.* **2022**, *5*, 11018–11024. [[CrossRef](#)]
9. Moon, Y.H.; Kim, N.Y.; Kim, S.M.; Jang, Y.J. Recent Advances in Electrochemical Nitrogen Reduction Reaction to Ammonia from the Catalyst to the System. *Catalysts* **2022**, *12*, 1015. [[CrossRef](#)]
10. Morales-Navas, C.; Martinez-Rodriguez, R.A.; Vidal-Iglesias, F.J.; Pena, A.; Soto-Perez, J.J.; Trinidad, P.; Solla-Gullon, J.; Tzvetkov, T.; Doan, J.; Smotkin, E.S.; et al. Autonomous electrochemical system for ammonia oxidation reaction measurements at the International Space Station. *NPJ Micrograv.* **2023**, *9*, 20. [[CrossRef](#)]
11. Habibzadeh, F.; Miller, S.L.; Hamann, T.W.; Smith, M.R., 3rd. Homogeneous electrocatalytic oxidation of ammonia to N₂ under mild conditions. *Proc. Natl. Acad. Sci. USA* **2019**, *116*, 2849–2853. [[CrossRef](#)] [[PubMed](#)]
12. Dunn, P.L.; Cook, B.J.; Johnson, S.I.; Appel, A.M.; Bullock, R.M. Oxidation of Ammonia with Molecular Complexes. *J. Am. Chem. Soc.* **2020**, *142*, 17845–17858. [[CrossRef](#)] [[PubMed](#)]
13. Sun, M.; Liu, J.; Song, C.; Ogata, Y.; Rao, H.; Zhao, X.; Xu, H.; Chen, Y. Different Reaction Mechanisms of Ammonia Oxidation Reaction on Pt/Al₂O₃ and Pt/CeZrO₂ with Various Pt States. *ACS Appl. Mater. Interfaces* **2019**, *11*, 23102–23111. [[CrossRef](#)] [[PubMed](#)]
14. Ruan, C.; Wang, X.; Wang, C.; Zheng, L.; Li, L.; Lin, J.; Liu, X.; Li, F.; Wang, X. Selective catalytic oxidation of ammonia to nitric oxide via chemical looping. *Nat. Commun.* **2022**, *13*, 718. [[CrossRef](#)]

15. Zott, M.D.; Peters, J.C. Enhanced Ammonia Oxidation Catalysis by a Low-Spin Iron Complex Featuring Cis Coordination Sites. *J. Am. Chem. Soc.* **2021**, *143*, 7612–7616. [[CrossRef](#)]
16. Zhao, Y.; Setzler, B.P.; Wang, J.; Nash, J.; Wang, T.; Xu, B.; Yan, Y. An Efficient Direct Ammonia Fuel Cell for Affordable Carbon-Neutral Transportation. *Joule* **2019**, *3*, 2472–2484. [[CrossRef](#)]
17. Guo, Y.; Pan, Z.; An, L. Carbon-free sustainable energy technology: Direct ammonia fuel cells. *J. Power Sources* **2020**, *476*, 228454. [[CrossRef](#)]
18. Gwak, J.; Choun, M.; Lee, J. Alkaline Ammonia Electrolysis on Electrodeposited Platinum for Controllable Hydrogen Production. *ChemSusChem* **2016**, *9*, 403–408. [[CrossRef](#)]
19. Xu, W.; Du, D.; Lan, R.; Humphreys, J.; Miller, D.N.; Walker, M.; Wu, Z.; Irvine, J.T.S.; Tao, S. Electrodeposited NiCu bimetal on carbon paper as stable non-noble anode for efficient electrooxidation of ammonia. *Appl. Catal. B Environ.* **2018**, *237*, 1101–1109. [[CrossRef](#)]
20. Herron, J.A.; Ferrin, P.; Mavrikakis, M. Electrocatalytic Oxidation of Ammonia on Transition-Metal Surfaces: A First-Principles Study. *J. Phys. Chem. C* **2015**, *119*, 14692–14701. [[CrossRef](#)]
21. Katayama, Y.; Okanishi, T.; Muroyama, H.; Matsui, T.; Eguchi, K. Enhancement of ammonia oxidation activity over Y₂O₃-modified platinum surface: Promotion of NH_{2,ad} dimerization process. *J. Catal.* **2016**, *344*, 496–506. [[CrossRef](#)]
22. Rosca, V.; Koper, M.T. Electrocatalytic oxidation of ammonia on Pt(111) and Pt(100) surfaces. *Phys. Chem. Chem. Phys.* **2006**, *8*, 2513–2524. [[CrossRef](#)]
23. Vidal-Iglesias, F.J.; Solla-Gullón, J.; Montiel, V.; Feliu, J.M.; Aldaz, A. Screening of electrocatalysts for direct ammonia fuel cell: Ammonia oxidation on PtMe (Me: Ir, Rh, Pd, Ru) and preferentially oriented Pt(100) nanoparticles. *J. Power Sources* **2007**, *171*, 448–456. [[CrossRef](#)]
24. Xu, W.; Lan, R.; Du, D.; Humphreys, J.; Walker, M.; Wu, Z.; Wang, H.; Tao, S. Directly growing hierarchical nickel-copper hydroxide nanowires on carbon fibre cloth for efficient electrooxidation of ammonia. *Appl. Catal. B Environ.* **2017**, *218*, 470–479. [[CrossRef](#)]
25. Tsai, M.-H.; Chen, T.-C.; Juang, Y.; Hua, L.-C.; Huang, C. High catalytic performance of CuCo/nickel foam electrode for ammonia electrooxidation. *Electrochem. Commun.* **2020**, *121*, 106875. [[CrossRef](#)]
26. Nagita, K.; Yuhara, Y.; Fujii, K.; Katayama, Y.; Nakayama, M. Ni- and Cu-co-Intercalated Layered Manganese Oxide for Highly Efficient Electro-Oxidation of Ammonia Selective to Nitrogen. *ACS Appl. Mater. Interfaces* **2021**, *13*, 28098–28107. [[CrossRef](#)] [[PubMed](#)]
27. Zhu, M.; Yang, Y.; Xi, S.; Diao, C.; Yu, Z.; Lee, W.S.V.; Xue, J. Deciphering NH₃ Adsorption Kinetics in Ternary Ni-Cu-Fe Oxyhydroxide toward Efficient Ammonia Oxidation Reaction. *Small* **2021**, *17*, e2005616. [[CrossRef](#)]
28. Zhang, S.; Yan, L.; Jiang, H.; Yang, L.; Zhao, Y.; Yang, X.; Wang, Y.; Shen, J.; Zhao, X. Facile Fabrication of a Foamed Ag₃Cu₂S₂ Film as an Efficient Self-Supporting Electrocatalyst for Ammonia Electrolysis Producing Hydrogen. *ACS Appl. Mater. Interfaces* **2022**, *14*, 9036–9045. [[CrossRef](#)]
29. Finkelstein, D.A.; Bertin, E.; Garbarino, S.; Guay, D. Mechanistic Similarity in Catalytic N₂ Production from NH₃ and NO₂⁻ at Pt(100) Thin Films: Toward a Universal Catalytic Pathway for Simple N-Containing Species, and Its Application to in Situ Removal of NH₃ Poisons. *J. Phys. Chem. C* **2015**, *119*, 9860–9878. [[CrossRef](#)]
30. Vidal-Iglesias, F.J.; Solla-Gullón, J.; Feliu, J.M.; Baltruschat, H.; Aldaz, A. DEMS study of ammonia oxidation on platinum basal planes. *J. Electroanal. Chem.* **2006**, *588*, 331–338. [[CrossRef](#)]
31. Oswin, H.G.; Salomon, M. The anodic oxidation of ammonia at platinum black electrodes in aqueous koh electrolyte. *Can. J. Chem.* **1963**, *41*, 1686–1694. [[CrossRef](#)]
32. Gerischer, H.; Mauerer, A. Untersuchungen Zur anodischen Oxidation von Ammoniak an Platin-Elektroden. *J. Electroanal. Chem. Interfacial Electrochem.* **1970**, *25*, 421–433. [[CrossRef](#)]
33. Gootzen, J.F.E.; Wonders, A.H.; Visscher, W.H.M.; Van Santen, R.A.; van Veen, J.A.R. A DEMS and cyclic voltammetry study of NH₃ oxidation on platinized platinum. *Electrochim. Acta* **1998**, *43*, 1851–1861. [[CrossRef](#)]
34. Xi, X.; Fan, Y.; Zhang, K.; Liu, Y.; Nie, F.; Guan, H.; Wu, J. Carbon-free sustainable energy technology: Electrocatalytic ammonia oxidation reaction. *Chem. Eng. J.* **2022**, *435*, 134818. [[CrossRef](#)]
35. Ye, J.-Y.; Lin, J.-L.; Zhou, Z.-Y.; Hong, Y.-H.; Sheng, T.; Rauf, M.; Sun, S.-G. Ammonia electrooxidation on dendritic Pt nanostructures in alkaline solutions investigated by in-situ FTIR spectroscopy and online electrochemical mass spectroscopy. *J. Electroanal. Chem.* **2018**, *819*, 495–501. [[CrossRef](#)]
36. Wei, R.-L.; Liu, Y.; Chen, Z.; Jia, W.-S.; Yang, Y.-Y.; Cai, W.-B. Ammonia oxidation on iridium electrode in alkaline media: An in situ ATR-SEIRAS study. *J. Electroanal. Chem.* **2021**, *896*, 115254. [[CrossRef](#)]
37. Kim, H.; Chung, M.W.; Choi, C.H. NO-induced deactivation of Pt electrocatalysis towards the ammonia oxidation reaction. *Electrochem. Commun.* **2018**, *94*, 31–35. [[CrossRef](#)]
38. Kutz, R.B.; Braunschweig, B.; Mukherjee, P.; Dlott, D.D.; Wieckowski, A. Study of Ethanol Electrooxidation in Alkaline Electrolytes with Isotope Labels and Sum-Frequency Generation. *J. Phys. Chem. Lett.* **2011**, *2*, 2236–2240. [[CrossRef](#)]
39. Ma, L.; Chu, D.; Chen, R. Comparison of ethanol electro-oxidation on Pt/C and Pd/C catalysts in alkaline media. *Int. J. Hydrogen Energy* **2012**, *37*, 11185–11194. [[CrossRef](#)]
40. Shih, Y.-J.; Huang, Y.-H.; Huang, C.P. Electrocatalytic ammonia oxidation over a nickel foam electrode: Role of Ni(OH)_{2(s)}-NiOOH_(s) nanocatalysts. *Electrochim. Acta* **2018**, *263*, 261–271. [[CrossRef](#)]

41. Lee, H.; Lee, J.-H.; Lee, Y.; Cho, E.-B.; Jang, Y.J. Boosting solar-driven N₂ to NH₃ conversion using defect-engineered TiO₂/CuO heterojunction photocatalyst. *Appl. Surf. Sci.* **2023**, *620*, 156812. [[CrossRef](#)]
42. Yang, Y.; Kim, J.; Jo, H.; Seong, A.; Lee, M.; Min, H.-K.; Seo, M.-g.; Choi, Y.; Kim, G. A rigorous electrochemical ammonia electrolysis protocol with in operando quantitative analysis. *J. Mater. Chem. A* **2021**, *9*, 11571–11579. [[CrossRef](#)]
43. Zhang, X.; Kong, R.M.; Du, H.; Xia, L.; Qu, F. Highly efficient electrochemical ammonia synthesis via nitrogen reduction reactions on a VN nanowire array under ambient conditions. *Chem. Commun.* **2018**, *54*, 5323–5325. [[CrossRef](#)] [[PubMed](#)]
44. Siddharth, K.; Alam, P.; Hossain, M.D.; Xie, N.; Nambafu, G.S.; Rehman, F.; Lam, J.W.Y.; Chen, G.; Cheng, J.; Luo, Z.; et al. Hydrazine Detection during Ammonia Electro-oxidation Using an Aggregation-Induced Emission Dye. *J. Am. Chem. Soc.* **2021**, *143*, 2433–2440. [[CrossRef](#)]
45. Li, L.; Tang, C.; Yao, D.; Zheng, Y.; Qiao, S.-Z. Electrochemical Nitrogen Reduction: Identification and Elimination of Contamination in Electrolyte. *ACS Energy Lett.* **2019**, *4*, 2111–2116. [[CrossRef](#)]
46. de Vooy, A.C.A.; Koper, M.T.M.; Van Santen, R.A.; van Veen, J.A.R. The role of adsorbates in the electrochemical oxidation of ammonia on noble and transition metal electrodes. *J. Electroanal. Chem.* **2001**, *506*, 127–137. [[CrossRef](#)]
47. Vidal-Iglesias, F.J.; Solla-Gullón, J.; Rodríguez, P.; Herrero, E.; Montiel, V.; Feliu, J.M.; Aldaz, A. Shape-dependent electrocatalysis: Ammonia oxidation on platinum nanoparticles with preferential (100) surfaces. *Electrochem. Commun.* **2004**, *6*, 1080–1084. [[CrossRef](#)]
48. Zhang, C.; Hwang, S.Y.; Peng, Z. Shape-enhanced ammonia electro-oxidation property of a cubic platinum nanocrystal catalyst prepared by surfactant-free synthesis. *J. Mater. Chem. A* **2013**, *1*, 14402–14408. [[CrossRef](#)]
49. Liu, J.; Zhong, C.; Yang, Y.; Wu, Y.T.; Jiang, A.K.; Deng, Y.D.; Zhang, Z.; Hu, W.B. Electrochemical preparation and characterization of Pt particles on ITO substrate: Morphological effect on ammonia oxidation. *Int. J. Hydrogen Energy* **2012**, *37*, 8981–8987. [[CrossRef](#)]
50. Sun, H.-Y.; Xu, G.-R.; Li, F.-M.; Hong, Q.-L.; Jin, P.-J.; Chen, P.; Chen, Y. Hydrogen generation from ammonia electrolysis on bifunctional platinum nanocubes electrocatalysts. *J. Energy Chem.* **2020**, *47*, 234–240. [[CrossRef](#)]
51. Martínez-Rodríguez, R.A.; Vidal-Iglesias, F.J.; Solla-Gullón, J.; Cabrera, C.R.; Feliu, J.M. Synthesis of Pt Nanoparticles in Water-in-Oil Microemulsion: Effect of HCl on Their Surface Structure. *J. Am. Chem. Soc.* **2014**, *136*, 1280–1283. [[CrossRef](#)] [[PubMed](#)]
52. Katsounaros, I.; Figueiredo, M.C.; Calle-Vallejo, F.; Li, H.; Gewirth, A.A.; Markovic, N.M.; Koper, M.T.M. On the mechanism of the electrochemical conversion of ammonia to dinitrogen on Pt(100) in alkaline environment. *J. Catal.* **2018**, *359*, 82–91. [[CrossRef](#)]
53. Pillai, H.S.; Xin, H. New Insights into Electrochemical Ammonia Oxidation on Pt(100) from First Principles. *Ind. Eng. Chem. Res.* **2019**, *58*, 10819–10828. [[CrossRef](#)]
54. Elnabawy, A.O.; Herron, J.A.; Karraker, S.; Mavrikakis, M. Structure sensitivity of ammonia electro-oxidation on transition metal surfaces: A first-principles study. *J. Catal.* **2021**, *397*, 137–147. [[CrossRef](#)]
55. Lomocso, T.L.; Baranova, E.A. Electrochemical oxidation of ammonia on carbon-supported bi-metallic PtM (M = Ir, Pd, SnOx) nanoparticles. *Electrochim. Acta* **2011**, *56*, 8551–8558. [[CrossRef](#)]
56. Sacré, N.; Duca, M.; Garbarino, S.; Imbeault, R.; Wang, A.; Hadj Youssef, A.; Galipaud, J.; Hufnagel, G.; Ruediger, A.; Roué, L.; et al. Tuning Pt–Ir Interactions for NH₃ Electrocatalysis. *ACS Catal.* **2018**, *8*, 2508–2518. [[CrossRef](#)]
57. Liu, Z.; Li, Y.; Zhang, X.; Rao, S.; Li, J.; Wang, W.; Sun, Z.; Yang, J. Surface Structure Engineering of PtPd Nanoparticles for Boosting Ammonia Oxidation Electrocatalysis. *ACS Appl. Mater. Interfaces* **2022**, *14*, 28816–28825. [[CrossRef](#)] [[PubMed](#)]
58. Endo, K.; Nakamura, K.; Katayama, Y.; Miura, T. Pt–Me (Me = Ir, Ru, Ni) binary alloys as an ammonia oxidation anode. *Electrochim. Acta* **2004**, *49*, 2503–2509. [[CrossRef](#)]
59. Siddharth, K.; Hong, Y.; Qin, X.; Lee, H.J.; Chan, Y.T.; Zhu, S.; Chen, G.; Choi, S.-I.; Shao, M. Surface engineering in improving activity of Pt nanocubes for ammonia electrooxidation reaction. *Appl. Catal. B Environ.* **2020**, *269*, 118821. [[CrossRef](#)]
60. Allagui, A.; Oudah, M.; Tuayev, X.; Ntais, S.; Almomani, F.; Baranova, E.A. Ammonia electro-oxidation on alloyed PtIr nanoparticles of well-defined size. *Int. J. Hydrogen Energy* **2013**, *38*, 2455–2463. [[CrossRef](#)]
61. Li, Y.; Li, X.; Pillai, H.S.; Lattimer, J.; Mohd Adli, N.; Karakalos, S.; Chen, M.; Guo, L.; Xu, H.; Yang, J.; et al. Ternary PtIrNi Catalysts for Efficient Electrochemical Ammonia Oxidation. *ACS Catal.* **2020**, *10*, 3945–3957. [[CrossRef](#)]
62. Du, X.T.; Yang, Y.; Liu, J.; Liu, B.; Liu, J.B.; Zhong, C.; Hu, W.B. Surfactant-free and template-free electrochemical approach to prepare well-dispersed Pt nanosheets and their high electrocatalytic activities for ammonia oxidation. *Electrochim. Acta* **2013**, *111*, 562–566. [[CrossRef](#)]
63. Bertin, E.; Garbarino, S.; Guay, D.; Solla-Gullón, J.; Vidal-Iglesias, F.J.; Feliu, J.M. Electrodeposited platinum thin films with preferential (100) orientation: Characterization and electrocatalytic properties for ammonia and formic acid oxidation. *J. Power Sources* **2013**, *225*, 323–329. [[CrossRef](#)]
64. Okanishi, T.; Katayama, Y.; Muroyama, H.; Matsui, T.; Eguchi, K. SnO₂-modified Pt electrocatalysts for ammonia-fueled anion exchange membrane fuel cells. *Electrochim. Acta* **2015**, *173*, 364–369. [[CrossRef](#)]
65. Katayama, Y.; Okanishi, T.; Muroyama, H.; Matsui, T.; Eguchi, K. Electrochemical Oxidation of Ammonia over Rare Earth Oxide Modified Platinum Catalysts. *J. Phys. Chem. C* **2015**, *119*, 9134–9141. [[CrossRef](#)]
66. Silva, J.C.M.; Piasentin, R.M.; Spinacé, E.V.; Neto, A.O.; Baranova, E.A. The effect of antimony-tin and indium-tin oxide supports on the catalytic activity of Pt nanoparticles for ammonia electro-oxidation. *Mater. Chem. Phys.* **2016**, *180*, 97–103. [[CrossRef](#)]

67. Zhou, Y.; Zhang, G.; Yu, M.; Wang, X.; Lv, J.; Yang, F. Free-Standing 3D Porous N-Doped Graphene Aerogel Supported Platinum Nanocluster for Efficient Hydrogen Production from Ammonia Electrolysis. *ACS Sustain. Chem. Eng.* **2018**, *6*, 8437–8446. [[CrossRef](#)]
68. Le Vot, S.; Roué, L.; Bélanger, D. Synthesis of Pt–Ir catalysts by coelectrodeposition: Application to ammonia electrooxidation in alkaline media. *J. Power Sources* **2013**, *223*, 221–231. [[CrossRef](#)]
69. Zhong, C.; Liu, J.; Ni, Z.; Deng, Y.; Chen, B.; Hu, W. Shape-controlled synthesis of Pt–Ir nanocubes with preferential (100) orientation and their unusual enhanced electrocatalytic activities. *Sci. China Mater.* **2014**, *57*, 13–25. [[CrossRef](#)]
70. Morita, S.; Kudo, E.; Shirasaka, R.; Yonekawa, M.; Nagai, K.; Ota, H.; Mikka, N.; Shiroishi, H. Electrochemical oxidation of ammonia by multi-wall-carbon-nanotube-supported Pt shell–Ir core nanoparticles synthesized by an improved Cu short circuit deposition method. *J. Electroanal. Chem.* **2016**, *762*, 29–36. [[CrossRef](#)]
71. Jiang, J. Promotion of PtIr and Pt catalytic activity towards ammonia electrooxidation through the modification of Zn. *Electrochem. Commun.* **2017**, *75*, 52–55. [[CrossRef](#)]
72. Lin, X.; Zhang, X.; Wang, Z.; Zhu, X.; Zhu, J.; Chen, P.; Lyu, T.; Li, C.; Tian, Z.Q.; Shen, P.K. Hyperbranched concave octahedron of PtIrCu nanocrystals with high-index facets for efficiently electrochemical ammonia oxidation reaction. *J. Colloid Interface Sci.* **2021**, *601*, 1–11. [[CrossRef](#)] [[PubMed](#)]
73. Li, Y.; Pillai, H.S.; Wang, T.; Hwang, S.; Zhao, Y.; Qiao, Z.; Mu, Q.; Karakalos, S.; Chen, M.; Yang, J.; et al. High-performance ammonia oxidation catalysts for anion-exchange membrane direct ammonia fuel cells. *Energy Environ. Sci.* **2021**, *14*, 1449–1460. [[CrossRef](#)]
74. Silva, J.C.M.; Ntais, S.; Teixeira-Neto, É.; Spinacé, E.V.; Cui, X.; Neto, A.O.; Baranova, E.A. Evaluation of carbon supported platinum–ruthenium nanoparticles for ammonia electro-oxidation: Combined fuel cell and electrochemical approach. *Int. J. Hydrogen Energy* **2017**, *42*, 193–201. [[CrossRef](#)]
75. Xue, Q.; Zhao, Y.; Zhu, J.; Ding, Y.; Wang, T.; Sun, H.; Li, F.; Chen, P.; Jin, P.; Yin, S.; et al. PtRu nanocubes as bifunctional electrocatalysts for ammonia electrolysis. *J. Mater. Chem. A* **2021**, *9*, 8444–8451. [[CrossRef](#)]
76. Kapałka, A.; Cally, A.; Neodo, S.; Comninellis, C.; Wächter, M.; Udert, K.M. Electrochemical behavior of ammonia at Ni/Ni(OH)₂ electrode. *Electrochem. Commun.* **2010**, *12*, 18–21. [[CrossRef](#)]
77. Zhang, S.; Zhao, Y.; Yan, L.; Jiang, H.; Yang, X.; Wang, Y.; Song, H.; Zhao, X. Electrochemical ammonia oxidation reaction on defect-rich TiO nanofibers: Experimental and theoretical studies. *Int. J. Hydrogen Energy* **2021**, *46*, 39208–39215. [[CrossRef](#)]
78. Zott, M.D.; Garrido-Barros, P.; Peters, J.C. Electrocatalytic Ammonia Oxidation Mediated by a Polypyridyl Iron Catalyst. *ACS Catalysis* **2019**, *9*, 10101–10108. [[CrossRef](#)]
79. Choueiri, R.M.; Tatarchuk, S.W.; Klinkova, A.; Chen, L.D. Mechanism of ammonia oxidation to dinitrogen, nitrite, and nitrate on β-Ni(OH)₂ from first-principles simulations. *Electrochem. Sci. Adv.* **2021**, *2*, 2100142. [[CrossRef](#)]
80. Allagui, A.; Sarfraz, S.; Baranova, E.A. Ni_xPd_{1-x} (x = 0.98, 0.93, and 0.58) nanostructured catalysts for ammonia electrooxidation in alkaline media. *Electrochim. Acta* **2013**, *110*, 253–259. [[CrossRef](#)]
81. Wang, R.; Liu, H.; Zhang, K.; Zhang, G.; Lan, H.; Qu, J. Ni(II)/Ni(III) redox couple endows Ni foam-supported Ni₂P with excellent capability for direct ammonia oxidation. *Chem. Eng. J.* **2021**, *404*, 126795. [[CrossRef](#)]
82. Jiang, K.; Li, K.; Liu, Y.-Q.; Lin, S.; Wang, Z.; Wang, D.; Ye, Y. Nickel-cobalt nitride nanoneedle supported on nickel foam as an efficient electrocatalyst for hydrogen generation from ammonia electrolysis. *Electrochim. Acta* **2022**, *403*, 139700. [[CrossRef](#)]
83. Jin, Y.; Chen, X.; Wang, J. From inert to active: A cocktail-like mediation of an Ag/Ni mixture for electrocatalytic ammonia oxidation reaction. *Chem. Commun.* **2022**, *58*, 10631–10634. [[CrossRef](#)] [[PubMed](#)]
84. Huang, J.; Chen, Z.; Cai, J.; Jin, Y.; Wang, T.; Wang, J. Activating copper oxide for stable electrocatalytic ammonia oxidation reaction via in-situ introducing oxygen vacancies. *Nano Res.* **2022**, *15*, 5987–5994. [[CrossRef](#)]
85. Hou, J.; Cheng, Y.; Pan, H.; Kang, P. CuSn Double-Metal Hydroxides for Direct Electrochemical Ammonia Oxidation to Dinitrogen. *ChemElectroChem* **2022**, *9*, e202101301. [[CrossRef](#)]
86. Huang, J.; Cai, J.; Wang, J. Nanostructured Wire-in-Plate Electrocatalyst for High-Durability Production of Hydrogen and Nitrogen from Alkaline Ammonia Solution. *ACS Appl. Energy Mater.* **2020**, *3*, 4108–4113. [[CrossRef](#)]
87. Yang, A.; Wang, J.; Su, K.; Lei, W.; Qiu, X.; Tang, Y. Modulating Hydroxyl-Rich Interfaces on Nickel-Copper Double Hydroxide Nanotyres to Pre-activate Alkaline Ammonia Oxidation Reactivity. *Chemistry* **2021**, *27*, 4869–4875. [[CrossRef](#)]
88. Song, J.; Yin Hai, Y.; Jia, Y.; Wang, T.; Wei, J.; Wang, M.; Zhou, S.; Li, Z.; Hou, Y.; Lei, L.; et al. Improved NH₃-N conversion efficiency to N₂ activated by BDD substrate on NiCu electrocatalysis process. *Sep. Purif. Technol.* **2021**, *276*, 119350. [[CrossRef](#)]
89. Wang, H.; Tong, X.; Zhou, L.; Wang, Y.; Liao, L.; Ouyang, S.; Zhang, H. Unique three-dimensional nanoflower-like NiCu electrodes constructed by Co, S co-doping for efficient ammonia oxidation reaction. *Sep. Purif. Technol.* **2022**, *303*, 122293. [[CrossRef](#)]
90. Almomani, F.; Bhosale, R.; Khraisheh, M.; Kumar, A.; Tawalbeh, M. Electrochemical oxidation of ammonia on nickel oxide nanoparticles. *Int. J. Hydrogen Energy* **2020**, *45*, 10398–10408. [[CrossRef](#)]
91. Zhang, H.; Chen, W.; Wang, H.; Tong, X.; Wang, Y.; Yang, X.; Wu, Z.; Liu, Z. A core-shell NiCu@NiCuOOH 3D electrode induced by surface electrochemical reconstruction for the ammonia oxidation reaction. *Int. J. Hydrogen Energy* **2022**, *47*, 16080–16091. [[CrossRef](#)]
92. Pillai, H.S.; Li, Y.; Wang, S.H.; Omidvar, N.; Mu, Q.; Achenie, L.E.K.; Abild-Pedersen, F.; Yang, J.; Wu, G.; Xin, H. Interpretable design of Ir-free trimetallic electrocatalysts for ammonia oxidation with graph neural networks. *Nat. Commun.* **2023**, *14*, 792. [[CrossRef](#)] [[PubMed](#)]

93. Song, L.; Liang, Z.; Ma, Z.; Zhang, Y.; Chen, J.; Adzic, R.R.; Wang, J.X. Temperature-Dependent Kinetics and Reaction Mechanism of Ammonia Oxidation on Pt, Ir, and PtIr Alloy Catalysts. *J. Electrochem. Soc.* **2018**, *165*, J3095–J3100. [[CrossRef](#)]
94. Fang, H.; Liao, C.; Ying, Y.; Cheng, J.; Wang, Q.; Huang, H.; Luo, Y.; Jiang, L. Creating metal-carbide interactions to boost ammonia oxidation activity for low-temperature direct ammonia fuel cells. *J. Catal.* **2023**, *417*, 129–139. [[CrossRef](#)]
95. Ma, H.; Schneider, W.F. Structure- and Temperature-Dependence of Pt-Catalyzed Ammonia Oxidation Rates and Selectivities. *ACS Catal.* **2019**, *9*, 2407–2414. [[CrossRef](#)]
96. Katsounaros, I.; Chen, T.; Gewirth, A.A.; Markovic, N.M.; Koper, M.T. Evidence for Decoupled Electron and Proton Transfer in the Electrochemical Oxidation of Ammonia on Pt(100). *J. Phys. Chem. Lett.* **2016**, *7*, 387–392. [[CrossRef](#)]
97. Skachkov, D.; Venkateswara Rao, C.; Ishikawa, Y. Combined First-Principles Molecular Dynamics/Density Functional Theory Study of Ammonia Electrooxidation on Pt(100) Electrode. *J. Phys. Chem. C* **2013**, *117*, 25451–25466. [[CrossRef](#)]
98. Jiang, X.; Ying, D.; Liu, X.; Liu, M.; Zhou, S.; Guo, C.; Zhao, G.; Wang, Y.; Jia, J. Identification of the role of Cu site in Ni-Cu hydroxide for robust and high selective electrochemical ammonia oxidation to nitrite. *Electrochim. Acta* **2020**, *345*, 136157. [[CrossRef](#)]

Disclaimer/Publisher's Note: The statements, opinions and data contained in all publications are solely those of the individual author(s) and contributor(s) and not of MDPI and/or the editor(s). MDPI and/or the editor(s) disclaim responsibility for any injury to people or property resulting from any ideas, methods, instructions or products referred to in the content.